JGR Space Physics

RESEARCH ARTICLE
10.1029/2023JA031654

Evolving Phase Propagation in an Intermediate-*m* ULF Wave Driven by Substorm-Injected Particles

C. M. Michael[1,2], T. K. Yeoman[2], D. M. Wright[2], M. A. Chelpanov[3], and P. N. Mager[3]

[1]Faculty of Arts, Science and Technology (FAST), University of Northampton, Northampton, UK, [2]School of Physics and Astronomy, University of Leicester, Leicester, UK, [3]Institute of Solar-Terrestrial Physics, Irkutsk, Russian Federation

Key Points:

- The case-study ultralow frequency wave, localized but with very long period, and with *m* number of ≈17 was simultaneously observed in the ionosphere by ground-based radar and on the Earth's surface by ground-based magnetometers
- The wave phase propagates eastward and appears to be driven by resonance with energetic electrons injected into the magnetosphere during a recent magnetospheric substorm
- The wave event is particularly unusual in that its latitudinal phase propagation characteristics appear to change during the event

Supporting Information:

Supporting Information may be found in the online version of this article.

Correspondence to:

C. M. Michael,
cm810@leicester.ac.uk;
chizurumokem@gmail.com

Citation:

Michael, C. M., Yeoman, T. K., Wright, D. M., Chelpanov, M. A., & Mager, P. N. (2024). Evolving phase propagation in an intermediate-*m* ULF wave driven by substorm-injected particles. *Journal of Geophysical Research: Space Physics*, *129*, e2023JA031654. https://doi.org/10.1029/2023JA031654

Received 1 MAY 2023
Accepted 19 FEB 2024

Abstract An ultralow frequency (ULF) wave was simultaneously observed in the ionosphere by the Super Dual Auroral Radar Network (SuperDARN) radar at Hankasalmi, Finland and on the ground by the International Monitor for Auroral Geomagnetic Effects (IMAGE) magnetometers with close proximity to the radar. The onset time of the wave event was around 03:00 magnetic local time. Fourier wave analysis of the event suggests a wave period of about 1,340 s with an equatorward latitudinal and eastward longitudinal wave phase propagation, and an effective azimuthal wave number of 17 ± 1, in the intermediate range of those observed in ULF waves. This wave has been interpreted as resulting from drifting electrons of energies of 13 ± 5 keV in a drift resonance condition linked to energetic particle populations during a magnetospheric substorm. The latitudinal phase characteristics of this wave experienced temporal evolution, believed to be caused by additional injected particle populations associated with the same substorm driving the wave, which resulted in an observed loss of HF backscatter. This observation of a unique type of temporal evolution in the phase propagation characteristics of ULF waves enhances current understanding about the structure, dynamics and source of these types of ULF waves.

Plain Language Summary The ultralow frequency (ULF) waves provide information about the Earth's global magnetic field known as magnetosphere. These waves contribute to the circulation of mass, energy and momentum in the near-earth space environment. However, the sources of these waves as well as the generation and propagation mechanisms behind them are not fully understood. In this paper, we have used Super Dual Auroral Radar Network (SuperDARN) radar and magnetometer observations to characterize a ULF wave event and investigate noticeable changes in the wave phase propagation over space and time during the wave event. The results show that the case-study ULF wave is localized with very long period. We find that the wave appears to be driven by resonance with energetic electrons injected into the magnetosphere by a process in the magnetosphere known as a substorm. We also find that the wave event is particularly unusual in that its phase propagation characteristics appear to change during the event. The results enhance current understanding of changes in the characteristics of ULF waves over space and time using a multi-instrument measurements.

1. Introduction

Ultralow frequency (ULF) waves are magneto-hydromagnetic waves that propagate through the Earth's magnetospheres with characteristic frequencies in the range of 1 mHz–10 Hz. These waves provide a conduit for energy and momentum transfer in the magnetosphere-ionosphere system (Yeoman et al., 2006). As such, they are an important diagnostic of magnetospheric structure and dynamics (Menk & Waters, 2013). Such waves are broadly classified based on their characteristic effective azimuthal wave number *m*, as low-*m* and high-*m* ULF waves. An azimuthal wave number strictly relies on the magnetic field geometry being azimuthally symmetric. Here an effective azimuthal wavenumber is defined only over a localized range of azimuth, and may well not apply across the full azimuthal range in more complicated geometries. The effective azimuthal wave number *m* of a ULF wave, also referred to as *m* number, is an important factor for determining the contribution of ULF wave-particle interactions to the dynamics internal to the magnetosphere (Murphy et al., 2018). The *m* number indicates the number of degrees of wave phase gradient per degree of magnetic longitude and it is inversely proportional to a ULF wave's azimuthal scale size. A common convention is that the sign preceding *m* number indicates the direction of the phase propagation of the wave. In this paper, positive *m* numbers denote waves with eastward phase propagation while negative *m* numbers are for waves with westward phase propagation.

ULF waves of the same *m* number spectrum tend to have similar wave mode and energy source and vice versa. For example, the low-*m* waves are generally thought to be from sources external to the magnetosphere such as the

solar wind, and they usually have an azimuthal scale structure that is large, with m numbers of ∼1 (Yumoto, 1988; Yeoman et al., 2006; Agapitov & Cheremnykh, 2013). The low-m waves primarily have toroidal polarization modes (e.g., Agapitov & Cheremnykh, 2013), but can also exist in non-Alfvénic modes from compression (Fenrich et al., 1995). For example, their source can be via resonance of the Earth's magnetic field line with the fast mode propagating through the magnetopause (e.g., Yeoman et al., 2006). Buffeting of the magnetosphere by variations in solar wind dynamic pressure can generate fast mode waves. Also, the rapid change in the solar wind velocity across the magnetopause can lead to processes such as the Kelvin-Helmholtz Instability (KHI) that can drive a fast compressional wave in the magnetosphere (Lessard et al., 1999; Rae et al., 2005). The compressional waves from KHI or buffeting can couple with field-aligned Alfvén waves when their frequencies match the natural frequencies of the field lines, driving toroidal Alfvén waves with a large azimuthal scale.

On the other hand, high-m ULF waves are poloidal modes with $m \sim 50$ and above, and are understood as being driven by sources internal to the Earth's magnetosphere (Klimushkin et al., 2019; Mager et al., 2019). For instance, energetic particles are deposited in the magnetotail through processes such as magnetospheric reconnection between the interplanetary and terrestrial magnetic fields, which could lead to a subsequent substorm activity. Such energetic particles enter into the inner magnetosphere and will experience gradient-curvature drift. These gradient-curvature drifting particles move around the Earth and as such form part of the global ring current. Also, these particles can drive MHD wave modes in the inner magnetosphere, resulting in perturbations in the electric and magnetic fields both in the magnetosphere and ionosphere when free energy is available to the wave. Such energy sources due to wave-particle interactions in the magnetosphere, commonly generate waves with high-m values or small azimuthal scale sizes.

High-m waves as described above can be excited by unstable particle populations by means of the drift-bounce or drift instability. Such unstable particles can be protons or electrons. Karpman et al. (1977) suggested that such unstable proton particles have energies of about 10–150 keV. ULF waves from such mechanisms can be due to a condition for which the part of the ion distribution function (IDF) feeds energy into the wave at the point where $\frac{\partial f}{\partial W} > 0$, with f representing the ion distribution function and W the energy (e.g., Hughes et al., 1978; Southwood, 1976). These non-Maxwellian IDFs also referred to as "bump-on-tail" distributions are created quite often by naturally-occurring processes in the magnetosphere. An example of such a process is a substorm-associated particle injection in the magnetosphere. Subsequent to such an injection, the ions will gradient-curvature drift in the westward direction while the electrons will drift in the eastward direction, and occasionally, the ions will match the local drift-bounce resonance condition (Southwood et al., 1969),

$$\omega_{wave} - m_{wave}\omega_d = N\omega_b \tag{1}$$

where the integer N is either zero in the case of a drift resonance or ±1 for drift-bounce resonance. The other parameters, ω_{wave}, m_{wave}, ω_d and ω_b in either cases are the angular frequency of the wave, the effective azimuthal wave number, the proton (or electron) azimuthal drift and the proton bounce angular frequencies respectively. Wave-particle interactions of this nature are a process of fundamental importance in collisionless astrophysical plasmas.

A previous study by Yeoman et al. (2010) grouped ULF waves ($10 < m < 20$) as intermediate-m ULF waves. The wave event reported in Yeoman et al. (2010) was linked to energetic particles injected by substorm activity and it exhibited an equatorward latitudinal phase propagation with a predominant poloidal mode. Such observational features are consistent with behaviors associated with high-m waves (e.g., Tian et al., 1991; Grant et al., 1992; Yeoman et al., 1992; Fenrich et al., 1995; Yeoman et al., 2008). As such, intermediate-m waves can be likened to high-m ULF waves, but with lower m values. Also, a recent study by Mager et al. (2019) reported a ULF wave event of 1.8 mHz, propagating westward in the ionosphere with m number of ∼10 as observed from a radar and the Van Allen Probes mission spacecraft data, which they ascribed to a drift-compressional mode due to substorm-injected proton particles with energy of about 90 keV leading to drift wave-particle resonance. In contrast, a ULF wave event with m number of 14 observed by Hao et al. (2014) was linked to interplanetary shock, which is a predominant generation mechanism for low-m waves. Thus, the generation mechanisms of these intermediate-m waves are yet to be fully understood.

ULF waves are observed both with ground based magnetometers and radars, and from in-situ spacecraft measurements. Using multi-instrument observations are very important for understanding the driving mechanism and

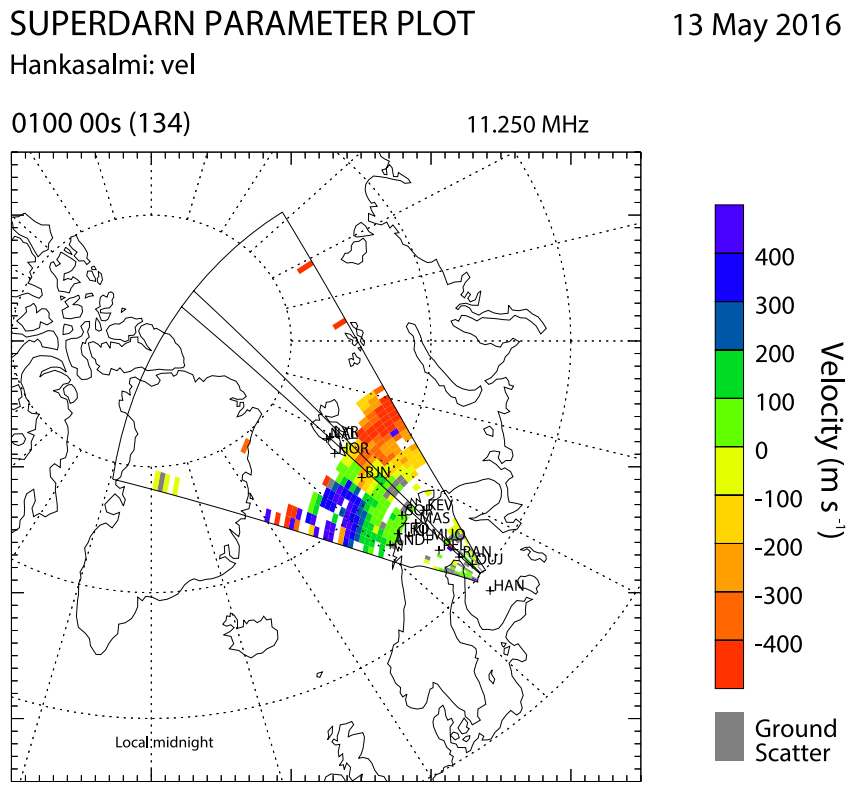

Figure 1. Field-of-view and data coverage from Channel A of the SuperDARN radar at Hankasalmi, Finland during the wave activity interval, onset at 01:00 UT in magnetic latitude-magnetic local time coordinates. The outline inside the FOV indicates the beam that Channel B is restricted to. The radial dashed lines are separated by 1 hr magnetic local time, with local midnight being marked by the vertical dashed line as highlighted. The positions of the IMAGE magnetometer stations used are highlighted. The ionospheric velocities are color-coded such that red (negative) and blue (positive) represent velocities away from the radar and toward the radar respectively.

structure of ULF waves, even though they are rare. For example, Mtumela et al. (2015) note that ground magnetometers and HF radars are synergistic instrument types for studying ULF waves.

In this study, we present an analysis of a ULF wave event simultaneously observed around 03:00 magnetic local time by the SuperDARN (Super Dual Auroral Radar Network) radar at Hankasalmi, Finland and ground-based magnetometer stations of the IMAGE (International Monitor for Auroral Geomagnetic Effects) array of magnetometers that are closely located in geomagnetic latitude and longitude with the Hankasalmi SuperDARN radar. The aim of this study is to investigate a possible evolution in the wave phase propagation behavior. An observational case study of a phase propagation transformation from a mostly poleward to equatorward wave propagation was reported in Chelpanov et al. (2019) for an intermediate-*m*. However, such observations of wave evolution are still rare. As such, the analysis presented here will contribute to a better understanding of the characteristic features of ULF waves and the processes driving them. The instruments, techniques and data used in this study are presented in the next section, followed by the analysis, discussion and summary.

2. Instrumentation and Data

The ionospheric convection velocities recorded by the SuperDARN (Super Dual Auroral Radar Network) radar at Hankasalmi, Finland were used to study the characteristics of ULF wave activity on 13th May 2016 as presented here. Figure 1 shows the fields-of-view (FOV) of the radar scan modes. SuperDARN radars typically use a 16 beam scanning routine, where each beam consists of 75 range gates with 3.24° beam separation. The Hankasalmi radar operated on two Channels A and B with the capability of utilizing a full 16-beam scan of 45 km range gates, starting at 180 km from the boresite of the radar. Further details of the operations of the SuperDARN radars can be found in (e.g., Chisham et al., 2007; Greenwald et al., 1995; Nishitani et al., 2019).

Table 1
The Geographic and Geomagnetic Location of the IMAGE Magnetometer Stations Used in This Study

S/N	Code	Name	Geo. lat. (°)	Geo. lon. (°)	CGM lat. (°)	CGM lon. (°)
1	NAL	Ny Ålesund	78.92	11.95	75.25	112.08
2	LYR	Longyearbyen	78.20	11.82	75.12	113.00
3	HOR	Hornsund	77.00	15.60	74.13	109.59
4	BJN	Bear Island	74.50	19.20	71.45	108.07
5	SOR	Sørøya	70.54	22.22	67.34	106.17
6	KEV	Kevo	69.76	27.01	66.32	109.24
7	TRO	Tromsø	69.66	18.94	66.64	102.90
8	MAS	Masi	69.46	23.70	66.18	106.42
9	AND	Andenes	69.30	16.03	66.45	100.37
10	KIL	Kilpisjärvi	69.06	20.77	65.94	103.80
11	MUO	Muonio	68.02	23.53	64.72	105.22
12	PEL	Pello	66.90	24.08	63.55	104.92
13	RAN	Ranua	65.90	26.41	62.09	105.91
14	OUJ	Oulujärvi	64.52	27.23	60.99	106.14
15	HAN	Hankasalmi	62.25	26.60	58.69	104.54

Note. CGM stands for Corrected Geomagnetic Coordinates. Taken from IMAGE (2019).

In this study, the Hankasalmi SuperDARN radar sounded its 16 beams, all pointing northwards on Channel A as outlined in Figure 1. Channel B was constrained to one beam across the entire range gates as highlighted inside the radar FOV outline. The oscillations in the velocity toward and away from the radar depict ULF wave activity. In this case, there is little ground scatter from range gates 24 up to 35 along the radar beams making the velocity data more suitable for wave analysis. The radar beam 9 has 3 s resolution, and is a focus of the study, but the wave is also investigated in beams 5–10, where it is most clearly observed, with a time resolution of 1 min. We also present here, magnetometer data obtained from the International Monitor for Auroral Geomagnetic Effects (IMAGE) database, with a sampling interval of 20 s. The positions of the IMAGE magnetometer stations used in this study with respect to the radar FOV, are illustrated in Figure 1 and their names and location coordinates are presented in Table 1.

3. Methods

The time-series radar velocity data were interpolated onto a uniform time axis, zero meaned and a 10% cosine bell applied before Fourier analysis was used to calculate the power and phase of the wave spectra. The data preparing process before the Fourier analysis has been used because the time series measurement of the ULF wave from SuperDARN is finite. As such, the ends of the time series data is tapered to reduce spectral leakage. In this case, we have used a cosine bell function with a 10% fixed fraction tapered from both ends of each time series data. After the data preparing process, the time series data is processed using a Fast Fourier Transform (FFT) to derive the spectral power and phase of the wave. The dominant wave frequency is determined as the point where Fourier power is highest in the power spectrum. An example of such power spectra figure has been added in the supporting information. The values of the wave Fourier power and phase derived at the dominant frequency were selected for examining latitudinal and longitudinal variation of the amplitude and phase characteristics of the ULF wave. The Fourier phase values selected from several range gates and beam combinations covering a range of geomagnetic longitudes at approximately constant (within ±0.5°) geomagnetic latitude were used to determine the wave's azimuthal phase propagation and the effective azimuthal wave number. The latitude extent between the first and the last radar range gates used in the latitudinal analysis is ∼8°. The phase is relative to the Fourier phase of a reference range gate. In the case of the magnetometer measurements, wave amplitude and phase values derived from stations with identical geomagnetic longitude but different latitude were used to study the latitudinal wave evolution and in the same vein for the longitudinal wave amplitude and phase variation. Magnetometer data of AND, TRO, KIL, MAS, KEV and SOR stations were used for examining the longitude profile of the ULF wave

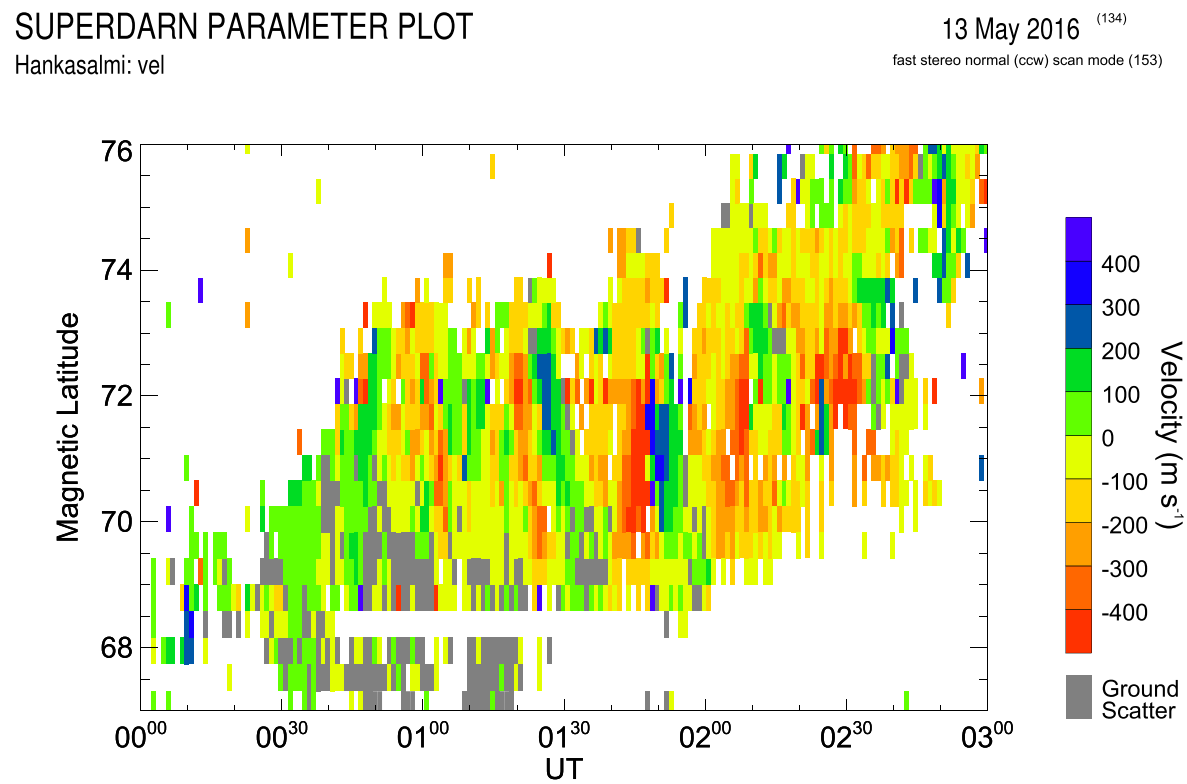

Figure 2. Hankasalmi beam 9 SuperDARN radar velocity measurements as a function of magnetic latitude. The ionospheric velocities are color-coded such that red (negative) and blue (positive) represent velocities away from the radar and toward the radar respectively.

observations and the rest of the stations presented in Table 1, except AND, MAS and KEV for the latitude profile. The effective azimuthal wave number was derived in a similar process as in the case of the radar observations.

4. ULF Wave Event on 13 May 2016

Figure 2 shows ionospheric flow velocities of the Hankasalmi radar beam 9 measurements of ULF wave activity that occurred on 13 May 2016. It displays the meridional view of the wave as a function of geomagnetic latitude, which corresponds to the radar range gates of about 20–40. The horizontal axis shows the time of the Hankasalmi SuperDARN radar coverage in universal time (UT). The ionospheric velocities across the radar fields of view during the time interval are color-coded such that red (negative) color indicates velocities away from the radar while blue (positive) color shows velocities toward the radar fields of view. The velocity flows between magnetic latitudes of 69° and 74° depict clear oscillations with a seeming equatorward phase propagation in the interval 00:00 UT to 01:30 UT, a wave signature associated with particle-driven ULF waves in a similar study of a ULF wave activity from SuperDARN radar measurements (Yeoman et al., 2010). However, the oscillatory flow velocities appeared to evolve into a poleward-like phase around the interval of 01:40 UT to 03:00 UT, more prominent in the component of the velocity flowing away from the radar. Another feature that can be observed is a loss of HF backscatter or HF data loss (Gauld et al., 2002) at about 01:40 UT and ∼72° latitude and L-shell of ∼10. This is more obvious in the next figure (Figure 3).

Figure 3 presents the velocity data for beams 3–9, in the same format as Figure 2, showing the temporal and spatial evolution of the HF data loss. The spatial extent of this HF data loss is further illustrated in the middle panel of Figure 4. Figure 4 presents the radar velocity measurements, similar to Figure 2, but for a constant time for each of the three panels. During the time of its appearance, the HF radar data loss area has a lower latitude limit of about 71° while the longitudinal width is ∼10°. As such, the data loss is located around 72° in latitude and the duration of this feature is ∼10 min. Such radar HF data loss can be attributed to depletion of scattering structure of the ionospheric irregularities region observed by the radar due to energetic particle precipitation from substorms, changes on HF propagation due to changing electron density, or ionospheric absorption (e.g., Gauld et al., 2002).

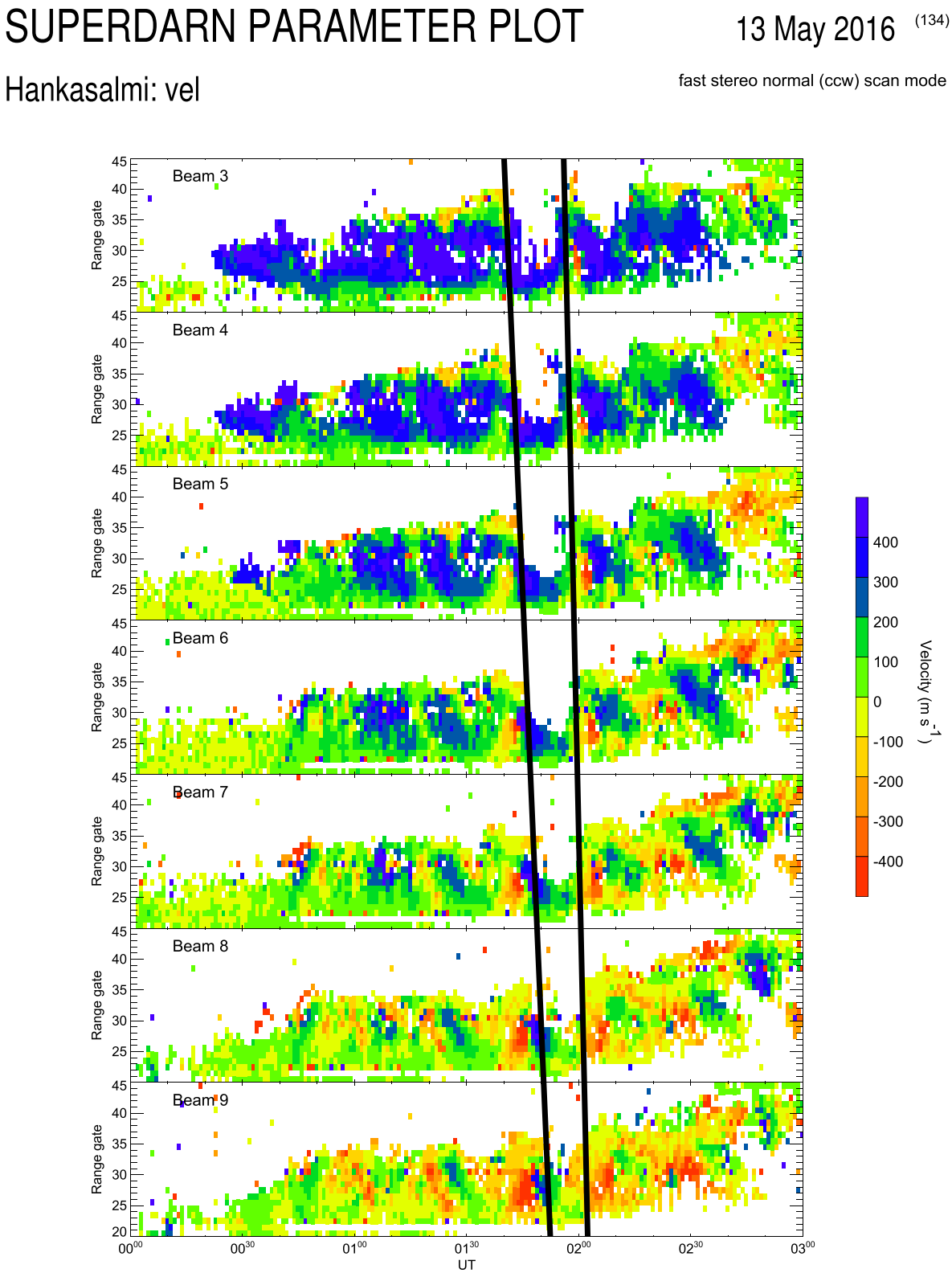

Figure 3. Hankasalmi beams 3–9 SuperDARN radar velocity measurements as a function of Radar range gate. The ionospheric velocities are color-coded such that red (negative) and blue (positive) represent velocities away from the radar and toward the radar respectively, while the black lines indicate drifting HF data loss features.

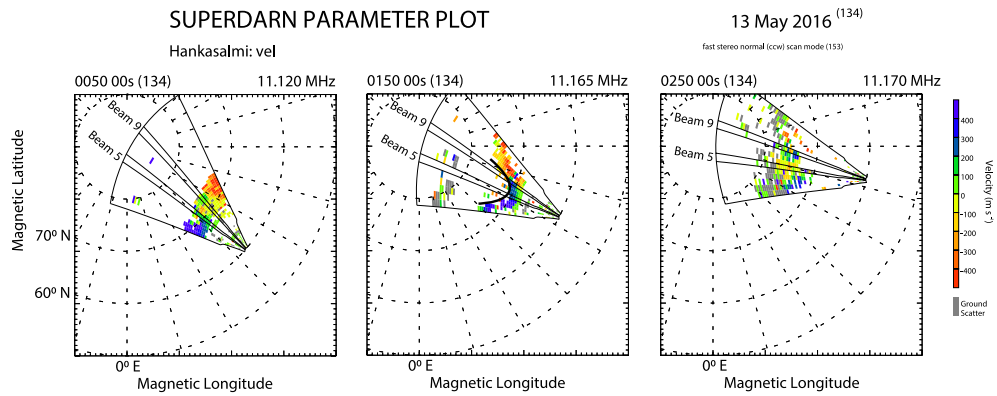

Figure 4. Similar to Figure 1 except that here shows wave activity onset at 00:50 UT before (left panel), 01:50 UT during (middle panel), and 02:50 UT after (right panel) the appearance of the HF data loss. The vertical outlines inside the FOV indicates beams 5 and 9 while curved black outline in middle panel describes the spatial extent of the HF data loss.

The spatial structure of the injected particles from such substorms can determine the phase characteristics of ULF waves driven by the substorm-injected particles (Yeoman et al., 2012). It is possible, following these past studies, that the phase evolution in the oscillatory flow velocities as seen in Figure 2 and the HF data loss depicted in Figure 3 might both be linked to energetic particles generated by substorms. These preliminary observations about this wave event are investigated further in the subsequent sections of this paper.

To understand the wave activity depicted by the oscillatory velocity flow in the range-time-velocity plots (such as the example shown in Figure 2), we have performed Fourier analysis following the method discussed in the previous section. The time series data of the wave activity from the radar velocity measurement cover a 3-hr (00:00–03:00 UT) interval on 13 May 2016. Here, the Fourier results obtained from the radar data over the 3-hr interval of this event are presented first. Thereafter, the 3-hr radar dataset is divided into two intervals to further investigate the wave's latitudinal phase propagation following the HF data loss and apparent evolution in the oscillatory flow velocities in the Hankasalmi SuperDARN radar measurements. Lastly, the results outlining substorm occurrence during the period of this wave event using magnetometer data are shown. Presented along with the magnetometer data is the Fourier analysis of a wave with similar frequency to the one observed in the radar data and another distinctive wave feature with a different frequency using the IMAGE magnetometer data.

Visualizing ULF wave activity from radar velocity data can be problematic due to data gaps in the interval of a wave event. Usually, this problem is rectified through velocity data reprocessing that involves interpolating the gaps. Excessive interpolation of data gaps can alter the wave features or produce a wrong result during Fourier analysis. As such, a check to confirm that there is sufficient data over a period of a wave event before Fourier analysis is important. To ensure sufficient data for Fourier analysis, data availability is ascertained for each of the 1,200 cells (i.e., 75 range gates multiplied by 16 beams) over the interval of wave activity. This procedure is demonstrated in Figure 5a, showing the percentage data occupancy in each cell during the interval.

In analyzing the present ULF wave events, we use cells with data availability of 50% and above for Fourier analysis to determine the amplitude and phase behavior of the wave. For example, as seen in Figure 2, key data required to analyze the 13th May 2016 activity measured by Hankasalmi radar are present as most gaps are at the start and end of the 3 hr length of the time-series data, part of which are tapered off before applying a Fast Fourier Transform (FFT). Likewise, while the right edges representing beams 14 to 16 do not meet the criteria as there are no cells with ≥50% data (green and blue cells) occupancy as seen in Figure 5a, beams 3 to about 11 consisting of the beams focused on here have sufficient data. The Fourier spectrum for each of the cells with ≥50% data was checked along with the time-series velocity, confirming that the unfavorable effect of data interpolation was insignificant and that the dominant frequency was present. Thus, the 50% criterion has been used because at this percentage there were sufficient data occupancy for each cell for Fourier analysis and also the spectra of each cell were examined to confirm that wave features were not altered.

Fourier analysis reveals a dominant frequency of 0.75 mHz. The 0.75 mHz dominant frequency is consistent between the latitude range of 68°–74° and longitude range of ~95°–110° across all the cells with ≥50% data

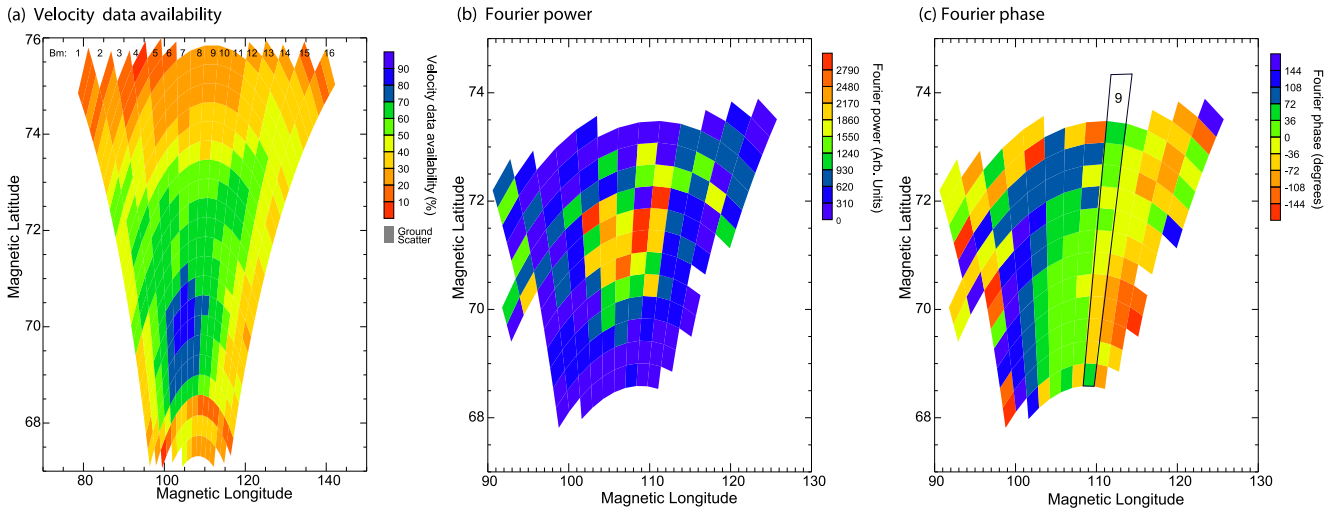

Figure 5. (a) Velocity data availability of the Hankasalmi SuperDARN radar velocity measurement of the 16 beams (e.g., Figure 2 shows measurement of beam 9). Color code shows percentage data occupancy in each cell over the 3-hr wave activity interval. Fourier (b) amplitude and (c) phase at 0.75 mHz peak frequency of the ULF wave derived from the ionospheric drift velocity measurement for all the cells with 50% and above data availability over the 3-hr (00:00–03:00 UT) interval across all the beams as a function of geomagnetic latitude and longitude. The black outline indicates beam 9.

occupancy as shown in Figure 5a. The dominant frequency of 0.75 mHz is about a 20 min period, which is consistent with the appearance of the time series of the oscillation in Figure 2. The wave frequency is referred to as the 0.8 mHz wave in subsequent analysis.

The Fourier amplitude and phase characteristics of the wave over the 3-hr interval is now examined in more detail. Figures 5b and 5c show the Fourier amplitude and phase characteristics of the wave at the dominant frequency of 0.75 mHz as a function of geomagnetic latitude and geomagnetic longitude. Each of the near-vertical columns of range cell data represents a beam, as highlighted by black outline for beam 9 which represents the beam used to examine the latitudinal phase profile. Figure 5b reveals a broad peak of the wave amplitude between the latitude range 70° and 72° and corresponding longitude range 102° and 112°. While Fourier phase calculated following the processes described in Section 3 varies from one range cell to another along the latitude range, the general trend mostly between beam 5 to about 10 (near-vertical columns around the outlined beam 9) where the wave activity is obvious, confirms an equatorward phase propagation over the 68°–74° latitude range. The phase propagation is equatorward where the phase values are decreasing with latitude as shown in Figure 5c. The latitudinal amplitude variation and phase propagation can also be viewed in a one-dimensional plot as shown in Figures 6a and 6b) along beam 9.

The longitudinal phase profile of the wave as shown in Figure 5c reveals an eastward phase propagation. This is indicated by a broad decrease in phase values from the west of longitude range (left) to the east of longitude range (right). Similarly, Figures 6c and 6d), which are the one-dimensional equivalent of Figures 5b and 5c) confirm an eastward phase propagation. Figures 6c and 6d) show the Fourier power and phase derived from the dominant frequency (0.75 mHz) across beams 5 to 11 (varying longitude) at radar range gate 25, which represents a constant latitude of ~70°. From Figure 6d, a corresponding effective azimuthal wave number, m of 17 ± 1 is calculated for this 0.8 mHz wave using linear least squares fit to the phase values as shown by the dotted lines in Figure 6d. This process has been used in previous studies for calculating effective azimuthal wave number (e.g., James et al., 2016).

The same process of determining the m number was repeated for radar range gates 27 and 30, which represent magnetic latitude ranges of ~71° and ~72° respectively. The differences in m values at those latitude ranges, representing the region with peak wave amplitude, are equal within uncertainty. The effective azimuthal wave number, m of 17 ± 1 calculated for this wave event represents an intermediate-m wave (e.g., Yeoman et al., 2010).

Furthermore, the longitudinal phase profile of the wave when viewed as a function of magnetic local time (Figure not shown here), clearly confirms an eastward phase propagation. As said earlier, in order to investigate the possible temporal latitudinal phase evolution of the ULF wave activity previously highlighted, the time series

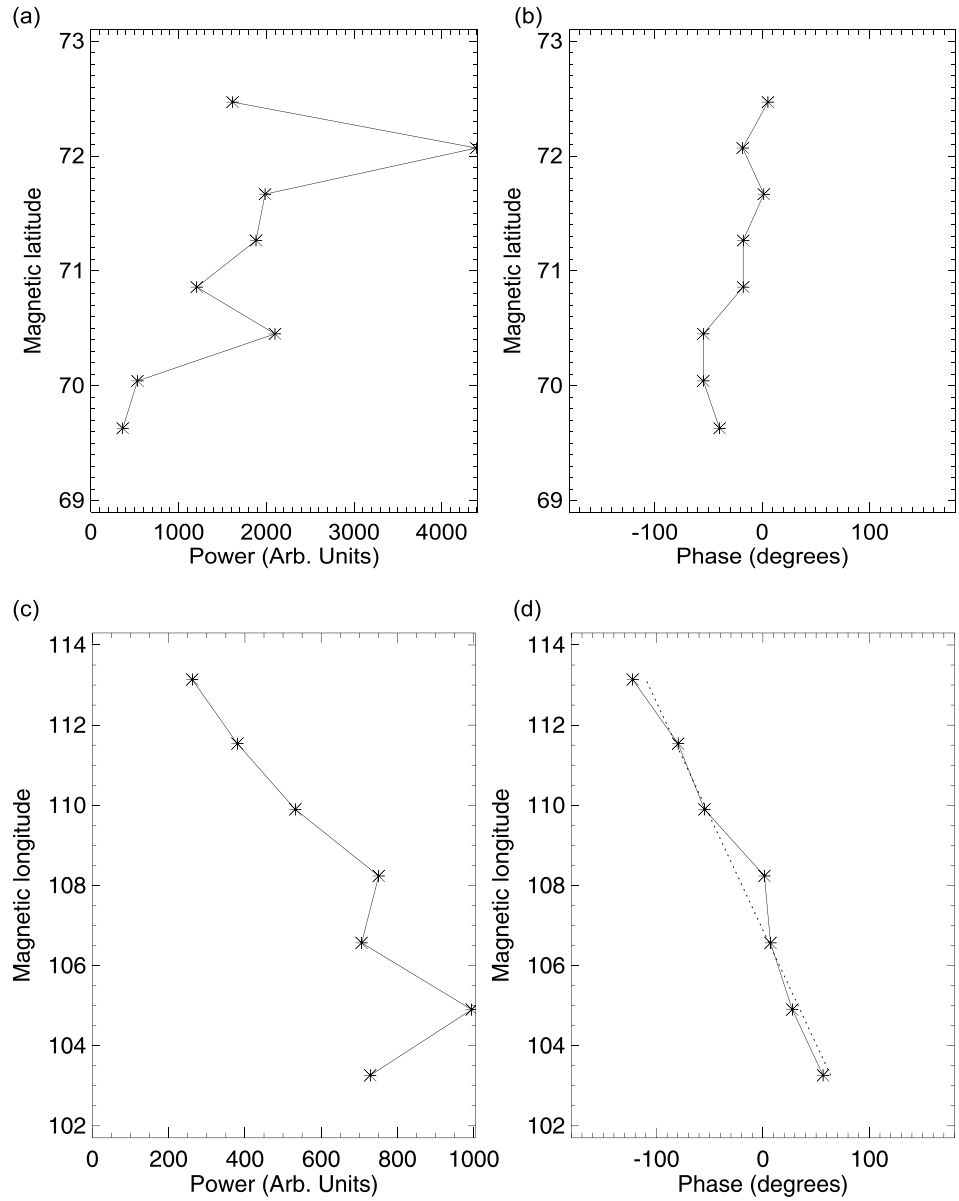

Figure 6. Fourier (a) amplitude and (b) phase at 0.75 mHz peak frequency of the ULF wave derived from the ionospheric drift velocity measurement along beam 9, and Fourier (c) amplitude and (d) phase across beams 5–11 of the Hankasalmi SuperDARN radar at ~70° latitude as a function of geomagnetic longitude. The dotted line in (d) is a linear fit to the longitudinal phase variation.

velocity data over the 3 hr of wave activity have been divided into two; 00:00 UT to 01:30 UT for Interval 1 analysis and 01:30 UT to 03:00 UT for Interval 2. We note that to do a more rigorous analysis of the possible evolution in the latitudinal phase propagation of the ULF wave would require longer radar data length, and for a better analysis, for example, would need a conjugate measurements from spacecraft. Unfortunately, we could only get the data that have been used for this study. Thus, the analysis for these two intervals investigating the possible phase evolution is presented in the next two sections.

4.1. Interval 1 (00:00–01:30 UT) Radar Observation

Fourier analysis of Interval 1 velocity data reveals that the same wave frequency of 0.8 mHz earlier described is detectable in Fourier spectra across the radar beams. The beams and range cells with ≥50% data occupancy and a clear wave activity features are used for the 2-dimensional Fourier amplitude and phase analysis (figure not

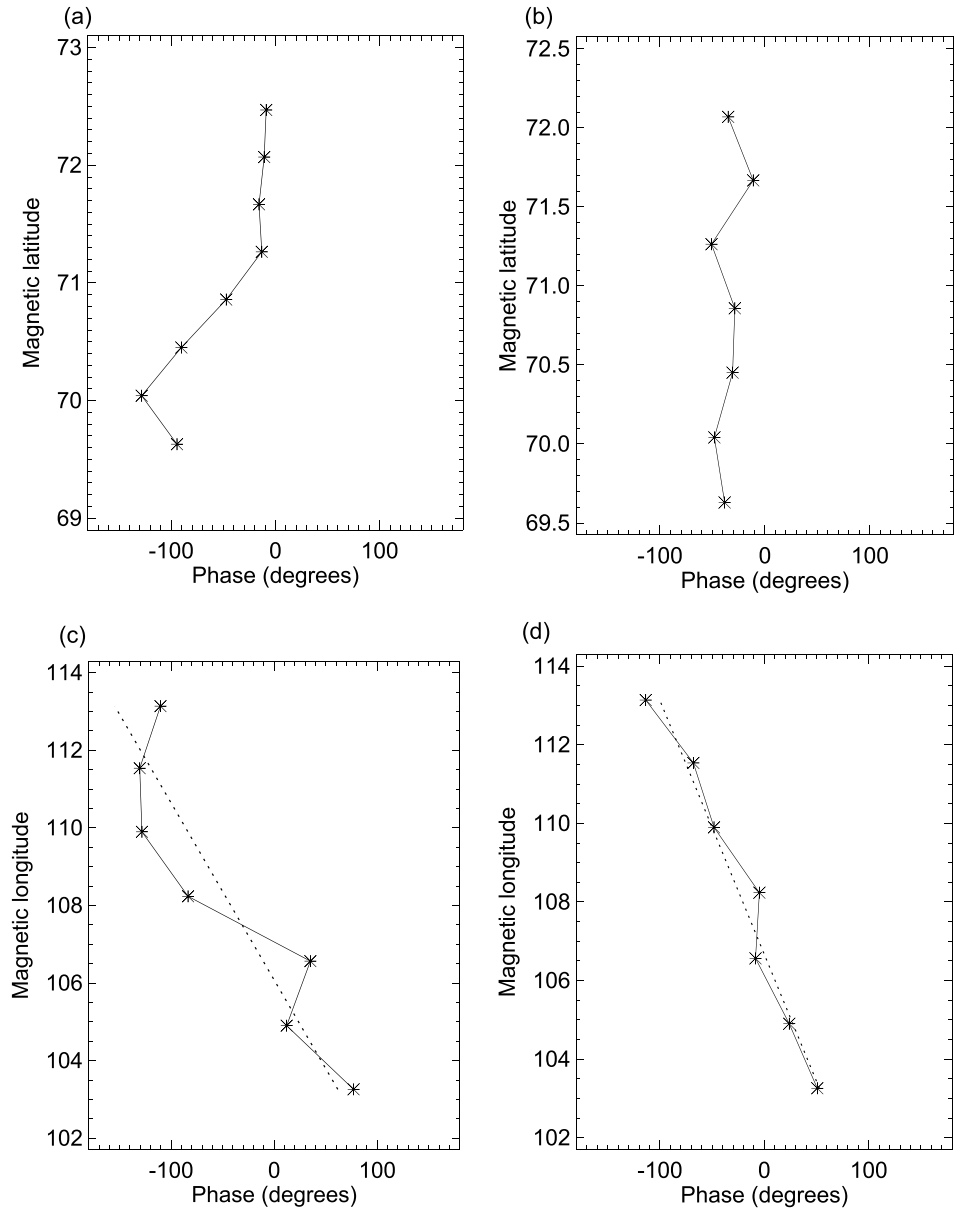

Figure 7. Fourier latitudinal phase profiles of the ULF wave derived from the ionospheric drift velocity measurement along beam 9 at (a) interval 1 and (b) interval 2. The equivalent longitudinal phase profiles of the ULF wave at (c) interval 1 and (d) interval 2. The longitudinal phase variations are calculated from 0.75 mHz frequency across beams 5–11 of the Hankasalmi SuperDARN radar at ∼70° latitude as a function of geomagnetic longitude. The dotted lines in (c) and (d) is a linear fit to the longitudinal phase variation used to calculate the *m* number.

shown here). The Fourier power from the ionospheric drift velocity measurements along the beams of interval 1 peaks at about 72° in latitude, while in longitude it peaks between ∼100° and 110°.

Latitudinal and longitudinal Fourier phase profiles for interval 1 are presented in Figures 7a and 7c. Whilst the phase propagation along beam nine is equatorward, some beams follow the same trend and others have mixed equatorward and poleward phase variation. The phase variation is considered to propagate equatorward where phase values are smaller at lower latitudes than at higher latitudes and it shows an equatorward phase variation, more obvious between 70° and 71° compared to the analysis over the 3-hr interval.

The longitudinal phase variation observed in interval 1 data generally indicates a clear eastward phase propagation. Following a similar effective azimuthal wave number calculation for the 3-hr wave observation, the *m*

number is examined for Interval 1 at latitude of ∼70°, which is equivalent to radar range gate 25, along beams 5–11 and, it is determined as 21 ± 3. The value for m is the gradient estimated using linear least squares fit to the phase values as shown by the dotted lines in Figure 7c. The eastward direction observed for the Interval one is consistent with the analysis for the 3-hr interval. However, the m value is slightly higher compared to the 3-hr interval analysis but still consistent within error, estimated from the standard error associated with the phase profile from the linear fit.

4.2. Interval 2 (01.30–03:00 UT) Radar Observation

In the last section, the wave behaviors at interval 1 showed a clearer equatorward latitudinal phase variation along beam 9 compared to the analysis over the 3-hr interval. Here, we repeat the same analysis but for interval 2 (01.30–03:00 UT). In a similar procedure to the previous time interval considerations, Fourier analysis was done where the percentage of data occupancy for each range cell across the beams meet the 50% criterion and have sufficient wave activity features. The same 0.8 mHz frequency is dominant as derived from Fourier spectra, similar to the analysis over the 3-hr of the wave activity. The wave amplitude peaks in latitude at about 72°, and in longitude between ∼102° and 111°, while the Fourier phase reveals little latitudinal phase propagation.

Figures 7b and 7d show the latitudinal phase profile and longitudinal phase profile of the 0.8 mHz wave for the interval 2. These plots are created following the processes discussed in Section 3. As seen in Figure 7b, the degree per latitude change of the wave phase variation over ∼69°–72° latitude range is small. The change in phase behavior seen in the time domain is not clearly illustrated through the Fourier analysis in Figure 7b given the short length of time of the Interval 2 available for analysis, but it is different from the other intervals. Fourier phase variation in magnetic longitude as seen in Figure 7d follows a similar eastward phase propagation with effective azimuthal wave numbers of 15 ± 1 determined using the same combination of radar range gate 25 (equivalent to ∼70° latitude) along beams 5–11. The m value is similar to that of the 3-hr interval and Interval 1.

5. Magnetometer Observations

Magnetic field data derived from the IMAGE magnetometer stations with close proximity to the Hankasalmi SuperDARN radar as presented in Table 1 have been employed to examine whether the wave observed by the radar is associated with a substorm, given that previous wave observations with a similar equatorward propagation in latitude and intermediate-m azimuthal properties were linked to substorm-generated particles (e.g., Yeoman et al., 2010). Also, the magnetometer measurements are examined for the signatures of the wave observed by the radar.

5.1. Substorm Occurrence

Figure 8 presents the unfiltered X-component of the IMAGE stations covering latitudes decreasing from top to bottom panels, with the last panel representing data from one of the stations (HAN, see Table 1) but band-pass filtered using a cut-off period between 20 and 200 s to emphasize Pi2 pulsation activity.

This figure shows that the interval between 18:00 UT and 20:10 UT on 12th May 2016 is magnetically quiet, followed by the onset of a substorm expansion phase characterized by sharp decrease in the X-component magnetic field at high latitudes, which is corroborated by the observation of a clear mid-latitude Pi2 pulsation. There are two clear subsequent Pi2 bursts around 20:50 UT and 23:30 UT on 12th May 2016. However, the substorm with the onset expansion phase at 20:10 UT may not be responsible for the wave activity detected by the Hankasalmi radar given the time lag of about 2.30 hr between the onset and the time (0000–0300 UT, 13 May 2016) that the wave activity was clearly observed in the radar data. As such, the subsequent bursts at about 20:50 UT and 23:30 UT are the likely substorm candidates that can drive the ULF wave observed in the radar.

Previous studies (e.g., James et al., 2016) have used ground-based magnetometer data to locate the substorm current systems, and we apply the same criteria here to identify the substorm current wedge location. The observed enhanced westward electrojet and substorm magnetic bay activity, up to −150 nT in the X-component data (equivalent here to the H-coordinate magnetic perturbation), confirm substorm occurrence and accompanying energetic particle injection at about 1-hr prior to the interval ULF wave activity is seen in the radar data. Data from ground-based magnetometer stations are also used to identify the substorm current wedge (SCW) as well as the azimuthal location of the substorm. This involves examining the background magnetic field variations

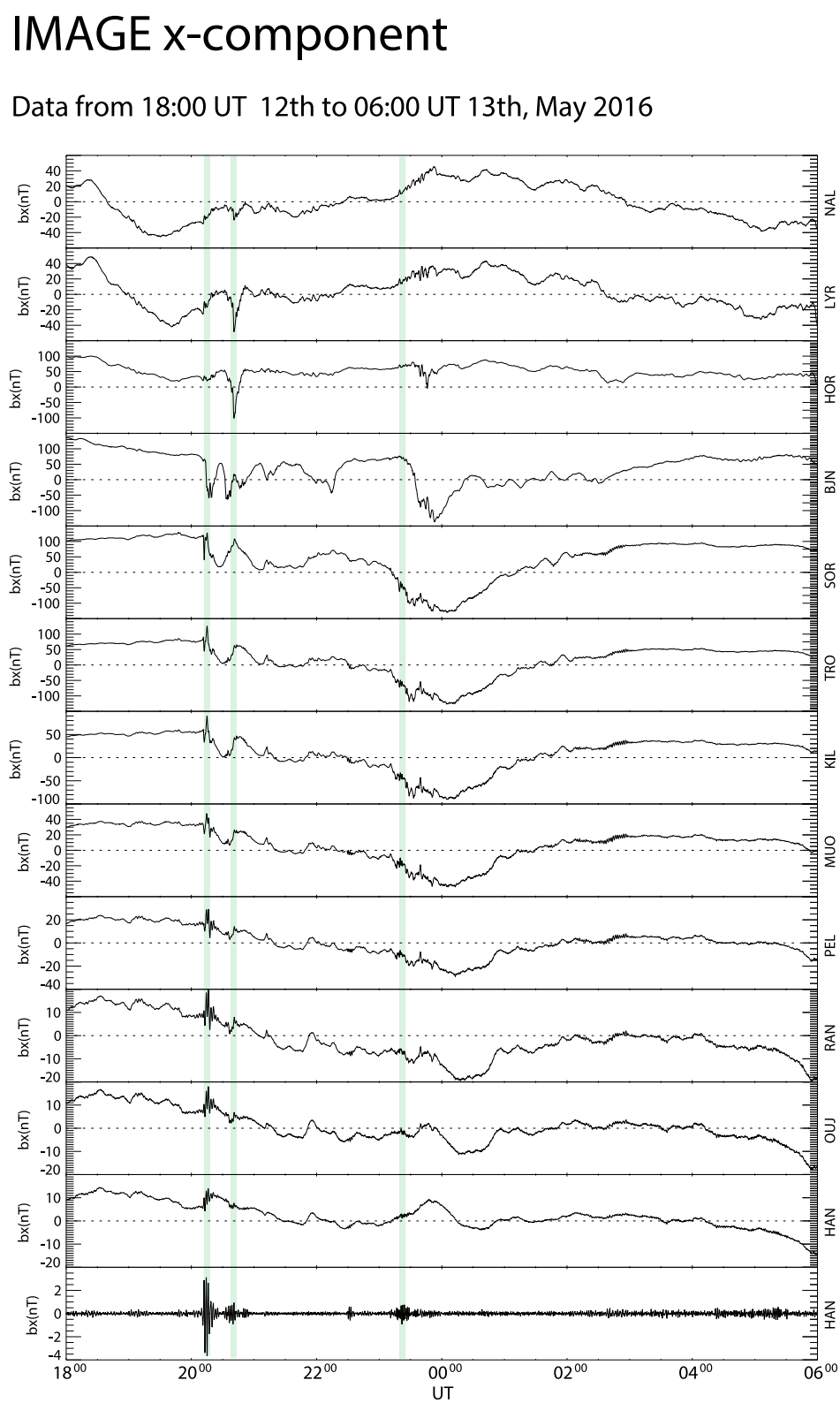

Figure 8. Unfiltered IMAGE X-component magnetometer data during the substorm interval. The IMAGE stations covering decreasing latitudes from top to bottom panels. The last panel shows HAN station data bandpass filtered between 20 and 200 s to highlight Pi2 pulsation activity. The light green outlines indicate onset of substorm expansion phase and subsequent bursts.

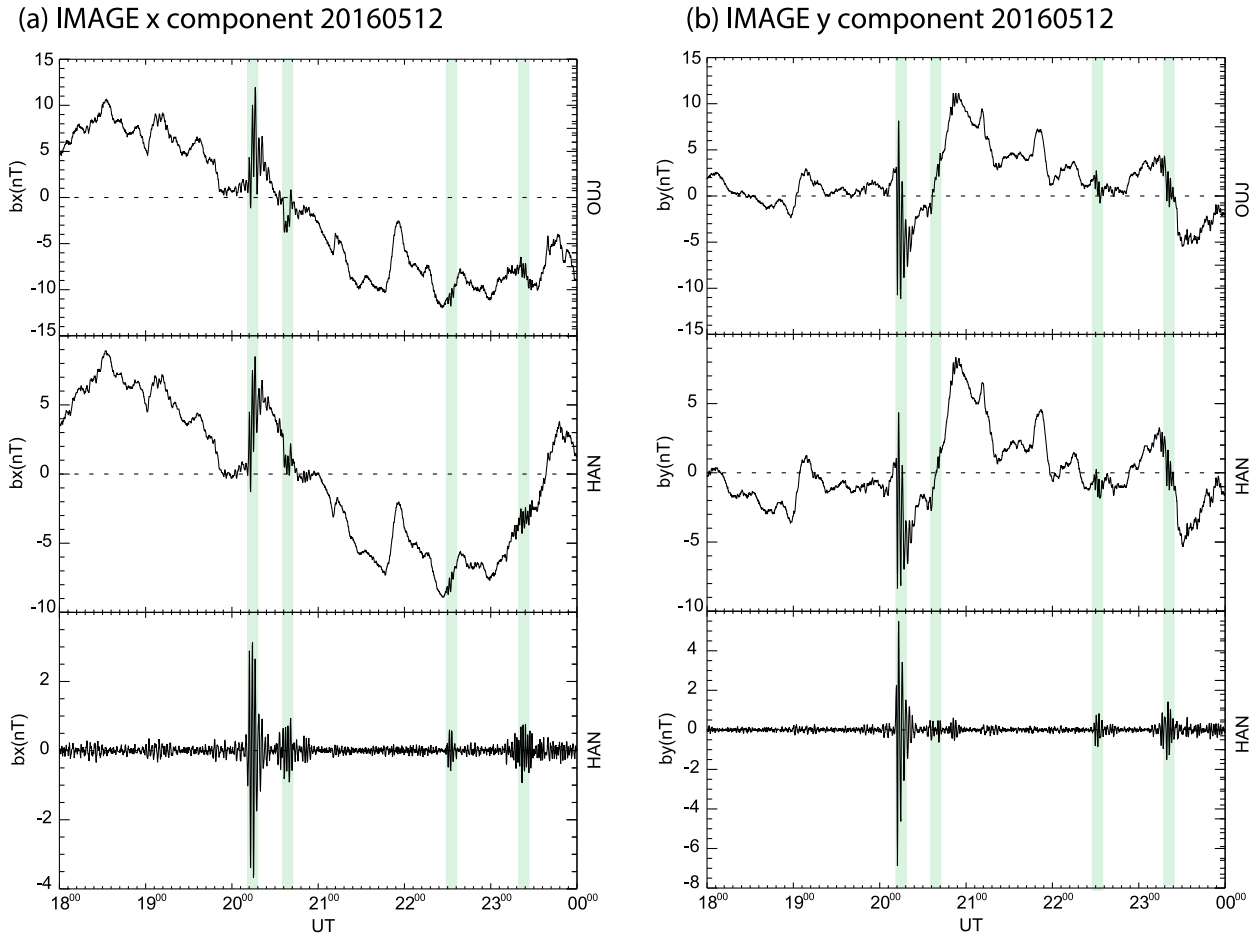

Figure 9. Magnetic field bay of mid-latitude IMAGE (a) X-component and (b) Y-components during the substorm. The data is the same as in previous Figure 8 and subsequent Figure 10 but for selected two mid-latitude stations between 18:00 and 23:59 UT interval on 12th May 2016. The top and middle panels are unfiltered X- and Y-components from the OUJ and HAN stations of the IMAGE array, while the bottom panels are HAN station but with a 200–20 s band-pass filter applied to illustrated the Pi2 pulsation activity (onset times marked with light green solid lines) associated with the substorm expansion phase onset at about 20:10 UT.

observed at the time of the Pi2 pulsations. Here, we used the large bays in the Y-component data to determine the location of the substorm current wedge. This process of using Pi2 wave appearance and associated magnetic bay disturbances in the midlatitude ground magnetometer data to detect the substorm current wedge location has been detailed in previous studies (e.g., Aylward et al., 1998; James et al., 2016; Kepko et al., 2015; Mann et al., 2008; Yeoman & Lühr, 1998).

We cannot precisely identify the substorm location with only ground magnetometers and also considering that the Atlantic lies to the west with no magnetometers in contrast to, for example, James et al. (2013), where they used substorms located by their auroral signatures. However, Figure 9 depicting a positive and negative bay in the mid-latitude X- and Y-component magnetic field respectively, suggests that the substorm is near and to the west of the IMAGE magnetometers. The variations of magnetic bays in the components of the geomagnetic field close to the substorm current wedge (SCW) can be used to deduce the location of the substorm (e.g., James et al., 2013). A decrease in the X-component coinciding with the Pi2 burst at higher latitude as shown previously in the top panels of Figure 8 indicates a westward electrojet. The upward and downward field-aligned currents from the SCW which feed this electrojet predict a symmetric peak in the X-component around the center of the SCW, and an asymmetric pattern in the Y-component at lower latitudes as highlighted in Figure 9. Thus, the mid-latitude X- and Y-component data here are consistent with a substorm close to the wave observations, but to the west. The role of energetic particle population from the substorm in generating the 0.8 mHz wave is considered in Section 6.1.

The Y-component of the magnetometer data as shown in Figure 10, reveals signatures of a long-period magnetic perturbation highlighted by light-blue outline and a seemingly narrowband short-period wave denoted by light-yellow outline. It is interesting to note here that the Y-component (east–west component at the earth's surface) of the magnetometer data is equivalent to north–south (direction of the Hankasalmi radar FOV) velocity of the ionospheric irregularities measured by the radar (Wright & Yeoman, 1999; Yeoman et al., 2016). Inspecting Figure 10 further, shows that for example, for the BJN station, there is a wave activity with a period of ∼1,350 s. This period is similar to the wave observed by the radar, which suggests that the magnetometers have detected the wave activity seen in the radar data. Furthermore, another distinct wave activity is seen around magnetometer stations such as SOR and TRO (see Figure 10), which is in the geomagnetic latitude range of 63°–68°. The distinct wave has a period of ∼120 s, which is within the frequency band of a Pc4 ULF wave (Jacobs et al., 1964). The wave is not visible in the high time resolution beam 9 radar data where data is restricted to latitudes above those of the magnetometers where the shorter period wave is observed, and we will not analyze this wave further here.

5.2. Magnetometer Observation of the 0.8 mHz ULF Wave

The IMAGE magnetometers have been employed to analyze the low frequency ULF wave characteristics observed between 00:00 and 03:00 UT on 13 May 2016 using Fourier analysis. As earlier stated, magnetometer and radar instruments complement each other. Thus, studying a wave event with both instruments will lead to an enhanced understanding of the wave behavior. Fourier spectra, calculated between 00:00 and 03:00 UT reveal a peak frequency of 0.77 mHz. This peak frequency observed in the magnetometer data is consistent with the initial inspection as well as being similar to the 0.75 mHz observed in the radar data, as such, it is subsequently referred to as the 0.8 mHz wave for consistency in naming. This is an indication that the same wave activity is detected in the ionosphere by the radar and on the earth's surface by closely located magnetometers.

Figures 11a and 11b) are latitudinal and longitudinal phase profiles for the magnetometer observations of the 0.8 mHz wave. The procedure used in creating this plots as well as calculating the effective azimuthal wave number are similar to the analysis for the radar observations as discussed in Section 3. The phase variation determined with Fourier analysis suggests a latitudinal phase gradient of ∼13.2° per degree in the equatorward direction, covering latitude range from 66.5° to ∼72° that is within the latitudinal range of the radar observation as depicted in Figure 11a.

In longitudinal phase variation shown in Figure 11b reveals an effective azimuthal wave number, m, of $\sim 16 \pm 1$ in the eastward direction. Note that the BJN station is the only magnetometer that lies close to the radar observations, as such, the wave behavior seen here from the magnetometer data is consistent with radar observations. However, we have not tried to split the wave in the same way that was possible with the radar data, due to the limited number of magnetometer stations available in the appropriate latitude range. Thus, the 0.8 mHz wave observed by ground-based IMAGE magnetometers with an equatorward phase propagation in latitude and eastward propagation in longitude (m number of $\sim 16 \pm 1$), have similar ULF wave characteristics to the wave observed in the radar.

6. Discussion

The oscillatory flow in the velocity data measured by the Hankasalmi SuperDARN radar on 13th May 2016 has been investigated for ULF wave activity using Fourier wave analysis as shown in the previous sections. In this section, we discuss the possible interpretations of the characteristic features observed for the case study ULF wave along with the magnetometer observations.

The wave activity studied using radar data between 00:00 and 03:00 UT is characterized by a frequency of 0.8 mHz. The total equatorward latitudinal phase variation shown in Figure 2 slightly exceeded 180° in the radar FOV. In addition, it is characterized by eastward longitudinal phase propagation with an intermediate-m effective azimuthal wave number (typically m ∼10 but less than 20) and a poloidal component. Equatorward phase propagation has been observed over part of the Hankasalmi radar FOV similar to the wave event observed by (e.g., Yeoman et al., 2008). Whilst the wave event in Yeoman et al. (2008) and wave events observed in (e.g., Grant et al., 1992; Yeoman et al., 1992) using other ground-based instruments have a small azimuthal scale size (high-m number), they are characterized by a westward longitudinal phase variation driven by drifting protons internal to the Earth's magnetosphere. Such observations of high-m waves propagating in westward direction are sparse compared to observations of low-m wave driven by external sources such as the solar wind. In contrast, the present observations of equatorward propagating ULF waves are more reminiscent based on wave's azimuthal

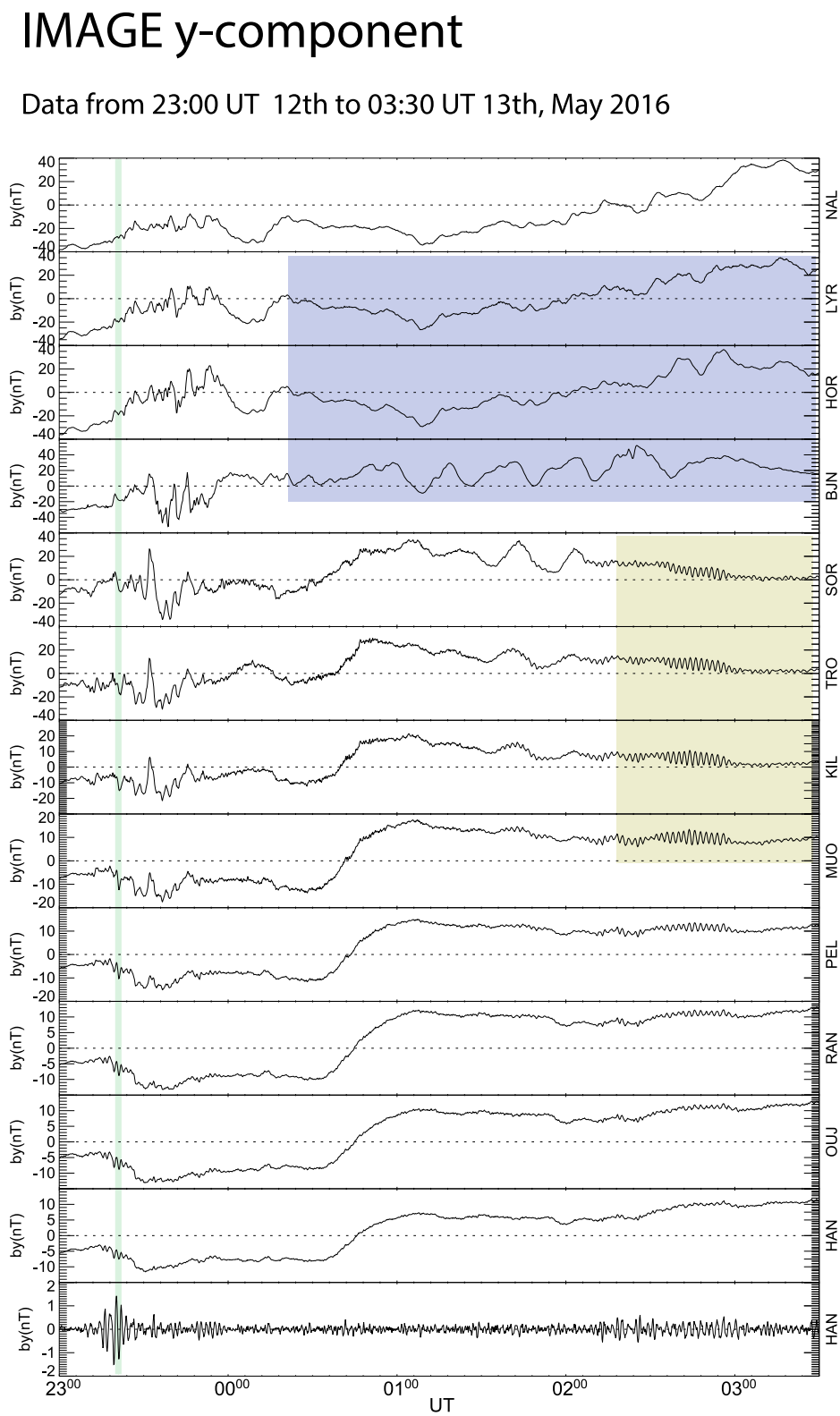

Figure 10. Similar to Figure 8 but for Y-component (east–west component at the earth's surface) and interval of 23:00 UT 12th to 03:30 UT 13 May 2016. The last panel shows HAN station data bandpass filtered between 20 and 200 s to highlight Pi2 pulsation activity indicated by the light-green outline. The light-blue and yellow highlight long period wave activity and short period wave respectively.

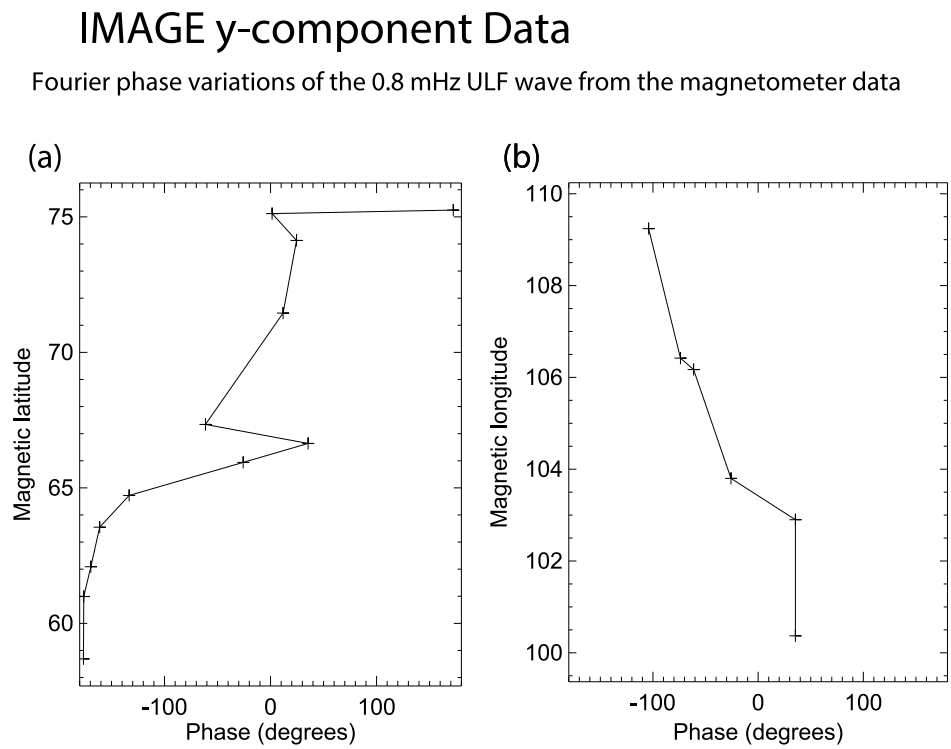

Figure 11. Latitudinal phase variation of the 0.8 mHz wave and the equivalent (b) longitudinal phase profile, both derived at 0.77 mHz peak Fourier spectra in the IMAGE Y-component magnetometer data between the interval 00:00–03:00 UT on 13 May 2016.

scale size (intermediate-*m* number) of waves observed by SuperDARN radars (Yeoman et al., 2010), Van Allen Probes spacecraft (Hao et al., 2014) and simultaneously using radar and spacecraft (Mager et al., 2019). However, the azimuthal direction found for the current wave is eastward, which is the same as Yeoman et al. (2010) but different from similar intermediate-*m* ULF waves propagating westward in Hao et al. (2014); Mager et al. (2019). Therefore, there might be a difference in excitation mechanism between the pulsation of the current case study and previous observations with intermediate-*m* number.

Data from Themis A (see https://cdaweb.gsfc.nasa.gov/) in the dusk sector shows evidence of dispersed ion signatures between $\sim 10 - 20$ keV close to 00:00 UT. Such westward-drifting ions have drift speeds of 10–30 min per hour of local time, and thus are thought to originate from a region westward of the wave observations, consistent with the inferred location of the substorm observed at ~23:30 UT which is interpreted here as providing the eastward drifting electrons that drive the wave activity. However, there are other generation mechanisms that can generate ULF waves (Agapitov & Cheremnykh, 2013). Various mechanisms also exist in the case of waves observed in the nightside region of the magnetosphere similar to this study. For example, shocks from the interplanetary region on the magnetosphere has been attributed to such waves (Hao et al., 2014). In addition, there are possibility of other mechanisms associated with the fluctuations in the solar wind dynamic pressure to generate these waves (e.g., Di Matteo et al., 2022; Motoba et al., 2003). However, we focus on the generation mechanism due to resonating particles injected into the magnetosphere in our discussion as we consider it to have shown the clearest plausibility in this case.

6.1. Driving Particles and Wave Energy

The dissimilarities in the driving mechanism ascribed to previous observations of intermediate-*m* waves (e.g., Yeoman et al., 2010; James et al., 2013; Hao et al., 2014; Mager et al., 2019) observed by radar and spacecraft, illustrates the complexities in predicting processes driving such a wave.

In the present case study, magnetic perturbations in the H coordinate system recorded at a number of IMAGE magnetometer stations having a close proximity with Hankasalmi radar, confirmed that there were various

substorm occurrences prior to the interval the waves are observed. One of such substorms occurred at ~23:30 UT on 12th May 2016, which was about 1 hr before time of the wave event. Due to the nearness of the substorm onset to the wave, there is a likelihood that energetic particles associated with the substorm might be driving the waves. This assumption is consistent with the interpretation of previous observations of intermediate and high-m waves with similar wave characteristics observed by satellites (Takahashi & McPherron, 1984) and ground-based radars (Baddeley et al., 2005; Yeoman et al., 2010). In such a case, the driving mechanism may be due to the drift or drift-bounce Alfvénic instability. This instability develops when particles with a given angular drift frequency resonantly exchange energy with waves (Southwood et al., 1969) as discussed further below. Note that the drift and drift-bounce resonance can involve protons and westward propagation while drift resonance only is possible for electrons and eastward propagation, due to the very rapid electron bounce. In addition, a similar intermediate-m wave reported by Yeoman et al. (2010) with equatorward latitudinal and eastward azimuthal phase propagation was associated with energetic electron generated by a substorm.

Following the substorm-particles being injected close to the time of wave observation, the energy associated with these particles can be determined for a better understanding of the wave characteristics. The driving particle energy is predicted using the drift-bounce resonance condition. Equation 1, described earlier, can be solved with respect to whether the driving particle is an electron or an ion. The pulsation event is assumed to have either a fundamental (symmetric, $N = 0$) or second harmonic (anti-symmetric, $N = 1$) standing wave structure. Based on these assumptions, the technique expressed in Chisham et al. (1992) and Chisham (1996) and applied by Yeoman et al. (2010) and also by Yeoman and Wright (2001); Baddeley et al. (2005) are followed in predicting the energy of the driving particles given that the effective azimuthal wave number derived for the 0.8 mHz wave observations and wave phase propagation are similar to Yeoman et al. (2010). Here we use the drift resonance approach for the 0.8 mHz wave given its eastward azimuthal propagation direction.

Following Baddeley et al. (2005), the angular drift frequency of interacting particles are determined using

$$\omega_{drift} = \frac{6WL(0.35 + 0.15\sin\alpha)}{B_s R_E^2} + \frac{2\Psi_0(0)L^3\sin\varphi}{B_s R_E^2} \quad (2)$$

where W represents the particle energy in eV and L is the particle's L-shell. The equation is based on a dipole magnetic field model (see Chisham, 1996), where B_s is the equatorial surface magnetic field strength, φ is the azimuth of particle measured anticlockwise from local midnight, α is the particle pitch angle, R_E is the Earth radius and $\Psi_0(0) \sim 45\left(1 - 0.159K_p + 0.0093K_p^2\right)^{-3}$ is the Volland-Stern (Stern, 1975; Volland, 1973) representation of the convective dawn to dusk electric potential. The first term on the right hand side of Equation 2 written as positive here is negative for ions. This term represents the gradient-curvature drift and so is in the opposite direction for ions (westward) and electrons (eastward), whereas the second term on the right hand side of Equation 2 is that resulting from $\mathbf{E} \times \mathbf{B}$ drift from the dawn to dusk electric field, and acts the same on both electrons and ions. But due to its relationship to sin φ it is positive (eastward) in the morning sector, and negative (westward) in the afternoon sector (and so contributes a drift component toward the dayside for both ions and electrons, irrespective of location) (Chisham, 1996).

The L-shell values used for the 0.8 mHz wave observation were in the range of 6.6–15, where the wave ranged, with a peak power at about $L = 10$, which was used for the calculation, while the pitch angles used were 90° when considering a drift resonance. As explained in Southwood and Kivelson (1982), drift resonance are likely to occur with particles of large pitch angles in the equatorial plane. The 0.8 mHz wave with eastward azimuthal phase propagation and equatorward phase motion is thought to be a fundamental poloidal mode (T. K. Yeoman & Wright, 2001). This coincided with the direction of gradient-curvature drifting electrons following substorm injection. The 0.8 mHz wave observed by the Hankasalmi SuperDARN radar, using Equations 1 and 2, is consistent with electrons drifting at an angular frequency of ~2.8×10^{-4} rad s^{-1}, corresponding to particle energies of 13 ± 5 keV for a drift resonance with error due to uncertainties in the parameters used (a range of L-shells between 7 and 10, pitch angles between 60 and 90° and the uncertainty in drift angular frequency from the radar data were input to Equations 1 and 2). Under these conditions, the drift resonance condition is satisfied, as such, the particles can provide energy to such a wave mode at the various interaction energies where a non-Maxwellian ion distribution function has a positive gradient, indicating that the free energy is available (Baddeley et al., 2002; Hughes & Southwood, 1976; Southwood, 1976).

Table 2
A Summary of the Characteristics of the 0.8 mHz ULF Wave Observations and a Previous ULF Wave Observations With Equatorward Phase Propagation

Study	Instrument	*m* number	Period	L-shell	W(keV)
This study	Radar	+17 ± 1	1,342	6.6–15	13 ± 5
	Magnetometer	+16 ± 1	1,294	6.6–15	13 ± 5
(Yeoman et al., 2010)	Radar	+13	580	7–15	33
(James et al., 2016) – Event 2	Radar	−12	1,440	9.08	8–19

The wave characteristics of the 0.8 mHz ULF wave observations have some similarities with previous wave studies as illustrated in Table 2. Electrons at the predicted drift angular frequency have a drift-time of ∼15 min per hour of Local Time (LT), which suggests that this wave is driven by particles associated with the final 23:30 UT substorm expansion seen in Figures 8 and 9.

6.2. Possible Evolution in Wave Phase Propagation

A possible evolution is seen in the phase characteristics of the 0.8 mHz wave activity observed by radar as shown in Figure 2. Initial investigation suggested that the wave evolved from an equatorward to poleward phase propagation, depicted by the velocity measurement away from the radar. The phase variation coincided with an eastward drifting HF data loss observed across the radar beams. The 3-hr dataset is subdivided into interval 1 and 2 to further examine the wave phase behavior. ULF wave driving mechanisms other than the drift-bounce instability explored in deriving the particle's energy as shown in the last section need to be considered to understand the possible phase evolution.

The investigation of a likely phase evolution seen in the ionospheric velocity data suggested that during Interval 1, the 0.8 mHz wave is mostly equatorward along Beam 9. The equatorward signature is clearer at this interval compared to the analysis over 3-hr. The azimuthal wave propagation was eastward, which is consistent with the analysis over the 3-hr interval. However, the *m* number is higher compared to the analysis over the 3-hr interval but within the uncertainties. On the other hand, the analysis of the Interval 2 produced a mostly mixed latitudinal phase propagation along the radar beams, with Beam 9 showing a poleward phase variation with a small gradient as well as azimuthal wave characteristics reminiscent of the 3-hr interval and Interval 1. Thus, there is a likelihood that the particle injection responsible for the HF data loss, which appeared at the beginning of Interval 2 resulted in the latitudinal phase transformation observed for the 0.8 mHz wave.

Such HF data loss has previously been associated with changes in the ionosphere due to particle precipitation from a substorm (Gauld et al., 2002). During such events the ionospheric electric field can be suppressed during the expansion phase of substorm, leading to data loss, because the plasma irregularities in the ionosphere responsible for the backscatter is reduced during this phase (Milan et al., 1999). Another mechanism suggested for the HF data loss is enhanced HF absorption in the D region ionosphere (e.g., Milan et al., 1996). However, Gauld et al. (2002) attributed the HF data loss observed in their study to changes in HF propagation resulting from changes in E and F region electron density. Such changes in the propagation conditions can cause a loss of backscatter resulting in an HF data loss as observed in the Hankasalmi SuperDARN radar measurement presented here.

In a similar substorm-driven ULF wave observed by Hankasalmi and Pykkvibær SuperDARN radars (Yeoman et al., 2010) following a moving wave source theory (e.g., Mager et al., 2009), it is suggested that the azimuthal separation of a substorm onset and a wave excitation due to particle population from the substorm influences the particle energy and effective azimuthal wave number. Also, this assumption has been corroborated by other studies (e.g., James et al., 2013). As such, lower energy particles (associated with higher-*m*) are due to bigger azimuthal separations between substorm onset and the wave.

The eastward drifting HF data loss feature is observed in the ionospheric plasma velocity flow across the Hankasalmi radar beams as earlier shown in Figure 3. Interestingly, the eastward direction of this HF data loss matches with the longitudinal phase propagation of the 0.8 mHz wave observed in both the radar and magnetometer data. Here, the measured azimuthal propagation of the data loss feature is compared with the calculated azimuthal propagation of the particles inferred from the wave observations, to establish whether the same energy

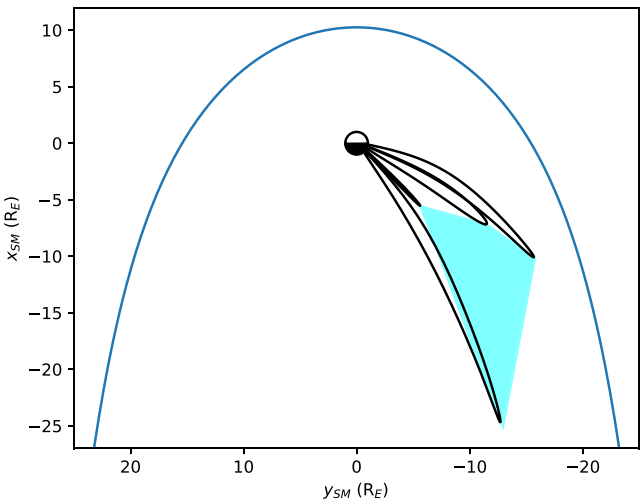

Figure 12. A first approximation to a trace plot for the ULF wave in the field of view of the Hankasalmi SuperDARN radar using the Tsyganenko, 1996 field model.

particles might be associated with both. Following the time interval that this feature is observed are signatures of latitudinal phase mixing and evolution observed in the radar data, more prominent in the velocities away from the radar. As noted earlier, this is an indication that the processes driving the wave might be responsible for the HF data loss. The velocity of the plasma flow associated with this feature has been determined from which the drifting particle energy is predicted. The time intervals between the onset and end of this feature for beam five is $t_2 - t_1$ and for beam nine is $t_4 - t_3$. The time gradient is estimated as 600 s with the longitudinal spatial gradient, $\Delta long$ between beam 5 and beam 9 giving 7.4°. A drift velocity corresponding to an angular frequency of 2.2×10^{-4} rad s^{-1} is determined by using

$$\frac{\Delta long \times \frac{\pi}{180}}{(t_4 - t_2) - (t_2 - t_1)} \quad (3)$$

This angular frequency is very similar to the predicted particle angular frequency of $\sim 2.8 \times 10^{-4}$ rad s^{-1} with energies of 13 ± 5 keV derived from the 0.8 mHz wave analysis. This provides a hint that the dynamic energetic particle interactions producing this HF data loss feature are responsible for the evolution of the wave activity observed by the Hankasalmi radar on 13th May 2016 from 00.00 UT to 03.00 UT.

Figure 12 presents the magnetic field lines, mapped using the Tsyganenko, 1996 magnetic field model Tsyganenko (1996), from the four corners of the observed backscatter region in Figure 2 into the Solar Magnetic equator. The shaded region between the equatorial crossing points of these field lines shows that the observed HF backscatter region maps into the dawnside magnetotail, covering a region from $L \sim 5$ to $L \sim 25$.

According to Klimushkin et al. (2004), Alfvén waves can transform from poloidal to toroidal polarisation and vice versa. The condition required for such transformation is detailed in (Klimushkin et al., 2004). Similarly, Radoski (1974); Mager and Klimushkin (2008); Zolotukhina et al. (2008); Mager et al. (2009); Elsden and Wright (2020) have demonstrated transformation of ULF wave activity between a mixed polarisation and poloidal. They showed theoretically that the wave transforms into a mixed polarization as it moves farther and farther away from the driving source. In addition, observational studies (e.g., Sarris et al., 2009), have shown such transformation of Alfvén waves from poloidal to toroidal polarisation and vice versa. In another previous study, Yeoman et al. (2012) observed a ULF wave event with a high-m and curved phase fronts, which they noted as a common action of the field line curvature, the plasma pressure and the equilibrium current, while some of the wave features agreed with a wave signature resulting from proton cloud drifting away from source in the magnetosphere. It was also shown in Chelpanov et al. (2018) that a significant fraction of long-period magnetospheric ULF pulsation observed in the ionosphere with radars has frequencies lower than appropriate Alfvén field line resonance frequencies. This agrees with previous studies showing that standing wave frequency of the outer magnetosphere can be lower than the fundamental standing Alfvén wave frequency (Dai et al., 2013; Takahashi et al., 2004, 2018). Such waves apparently have kinetic nature and can presumably represent the drift compressional mode. Properties of the wave are in agreement with this interpretation, although latitudinal propagation of this mode is not clear due to the lack of theory. In another previous study, Chelpanov et al. (2019) reported a wave event observed by radar that transformed from a poleward to equatorward phase propagation. They attributed the wave mode to a drift-compressional mechanism described in (Chelpanov et al., 2016; Kostarev & Mager, 2017). In the case of Mager et al. (2009), which considered a wave propagating equatorward in latitude, the azimuthally drifting particle inhomogeneity injected during substorm activity was suggested as a likely excitation mechanism for an azimuthal direction of the phase velocity that coincides with the cloud of energetic particles from the substorm. Consequently, the equatorward phase propagation observed here, which is thought to be resulting from the spatial structure of the driving particles might be accompanied by an evolving wave polarisation as the particle populations themselves evolve. However, such an evolution of the wave polarisation would not obviously transform the latitudinal phase propagation from poleward to equatorward. On the other hand, new particle populations are a candidate for transforming the wave polarisation going by energetic

particle interactions producing this HF data loss. We investigate the ground magnetometer wave signature further in the following sections.

6.3. Ground Magnetometer Wave Signature

In the magnetometer data, a wave was detected with a frequency similar to the 0.8 mHz wave observed by the Hankasalmi radar. In addition, this 0.8 mHz wave observed in the magnetometer data followed a similar equatorward latitudinal phase propagation as well as an eastward azimuthal propagation. The effective azimuthal wave number at 70° is 16 ± 1, which is slightly less than 17 ± 1 derived for the radar observation at the same latitude. This slight disparity in m number of the pulsation in the ionosphere as seen by Radar and on the Earth's surface measured by magnetometer might be due to attenuation of wavefield by the ionospheric currents as described in (e.g., Hughes & Southwood, 1976). Such attenuation as shown by Hughes and Southwood (1976), is proportional to e^{-kz} where k is the field-perpendicular component of the wave number and z is the E-region height of the ionosphere. Due to ionospheric screening, the attenuation factor has to be small in order for the waves to be detected on the ground by magnetometers. Whilst ULF waves with a high m number have been simultaneously detected in the ionosphere by radar and in ground magnetometer data (e.g., Yeoman et al., 2012; Mtumela et al., 2015), such multi-instrument observations of intermediate-m and high-m waves are sparse. The same particle energy predicted for the 0.8 mHz wave observed by the radar is applicable for the magnetometer data, clearly indicating that the same wave activity was observed simultaneously in the radar and magnetometer data.

7. Summary

ULF wave activity observed by the Hankasalmi SuperDARN radar, as well as detected in the data of IMAGE magnetometers with close proximity to the radar has been studied using Fourier wave analysis. Denoted as a 0.8 mHz pulsation, this wave followed an equatorward phase propagation in latitude and an eastward azimuthal propagation with an average m number of 17 ± 1 making it an intermediate-m class of ULF wave according to Yeoman et al. (2010). The 0.8 mHz wave reported here is believed to be due to drifting energetic electrons via a kinetic instability caused by the non-Maxwellian electron distribution functions, commonly termed "bump-on-tail" distributions similar to proton distribution functions reported by (e.g., Baddeley et al., 2005). The generation mechanism is thought to be a drift resonance ($N = 0$) wave-particle interaction (Southwood, 1976). On the other hand, the features of phase evolution observed by the radar may be due to an additional electron cloud drifting azimuthally in the magnetosphere. These additional energetic electrons are thought to be responsible for the evolving temporal latitudinal phase propagation, which is supported more by another possible ULF wave interpretation, the moving source theory of Mager and Klimushkin (2007); Mager and Klimushkin (2008), which a similar case study of an intermediate-m wave by Yeoman et al. (2010) adopted as a candidate for driving the wave event in their work. Other mechanisms behind the transformation and mixing of ULF wave polarisation are addressed by previous studies (e.g., Klimushkin et al., 2004; Mager & Klimushkin, 2008; Zolotukhina et al., 2008; Mager et al., 2009).

Furthermore, an HF data loss drifting azimuthally in the same eastward direction as the 0.8 mHz wave is observed in the ionospheric plasma velocity flow across the Hankasalmi radar beams. It is thought that the dynamic energetic particle interactions producing this data loss feature might have triggered the temporal latitudinal phase evolution observed during the 0.8 mHz wave activity by the Hanksalmi radar.

The ULF wave analysis presented here has shown interesting features. For example, the phase evolution believed to be associated with the HF data loss may be a one-off event or a more common feature in such intermediate-m waves. Therefore, statistical analysis of similar wave events observed in radar measurements will be useful in confirming these possibilities. Observations of intermediate to high-m ULF waves by radar and magnetometer are rare, making the case study presented here a useful analysis for further scientific understanding of this type of wave.

Data Availability Statement

The raw SuperDARN data used in this paper can be obtained from (http://vt.superdarn.org/). The IMAGE magnetometer data used in this paper are freely available and can be found at (http://space.fmi.fi/image/beta/).

Acknowledgments
C.M.M. was supported by TETFund (Ref. FUO/APRA/TETF.ASTD/14/15/002). T. K.Y. was supported by STFC UKRI Grant ST/W00089X/1 and NERC UKRI Grant NE/V000748/1. The work of M.A.C. and P.N.M. were financially supported by the Ministry of Science and Higher Education of the Russian Federation. C.M.M. would like to acknowledge the helpful suggestions from Gareth Chisham and Suzie Imber in the thesis version of the work presented here. The authors acknowledge the use of SuperDARN data. SuperDARN is a collection of radars funded by national scientific funding agencies of Australia, Canada, China, France, Italy, Japan, Norway, South Africa, United Kingdom and the United States of America. We would also like to acknowledge the IMAGE magnetometer team for providing the data. This research used the SPECTRE High Performance Computing Facility at the University of Leicester.

References

Agapitov, O., & Cheremnykh, O. (2013). Magnetospheric ULF waves driven by external sources. *Advances in Astronomy and Space Physics*, *3*, 12–19.

Aylward, A., Bucher, S., Pajunpää, A., Pajunpää, K., Holmboe, T., & Zalewski, S. (1998). Westward moving dynamic substorm features observed with the IMAGE magnetometer network and other ground-based instruments. *Annales Geophysicae*, *16*(4), 425–440. https://doi.org/10.1007/s005850050613

Baddeley, L. J., Yeoman, T. K., & Wright, D. M. (2005). HF Doppler sounder measurements of the ionospheric signatures of small scale ULF waves. *Annals of Geophysics*, *23*(5), 1807–1820. https://doi.org/10.5194/angeo-23-1807-2005

Baddeley, L. J., Yeoman, T. K., Wright, D. M., Davies, J. A., Trattner, K. J., & Roeder, J. L. (2002). Morning sector drift-bounce resonance driven ULF waves observed in artificially-induced HF radar backscatter. *Annals of Geophysics*, *20*(9), 1487–1498. https://doi.org/10.5194/angeo-20-1487-2002

Chelpanov, M. A., Mager, O. V., Mager, P. N., Klimushkin, D. Y., & Berngardt, O. I. (2018). Properties of frequency distribution of pc5-range pulsations observed with the Ekaterinburg decameter radar in the nightside ionosphere. *Journal of Atmospheric and Solar-Terrestrial Physics*, *167*, 177–183. https://doi.org/10.1016/j.jastp.2017.12.002

Chelpanov, M. A., Mager, P. N., Klimushkin, D. Y., Berngardt, O. I., & Mager, O. V. (2016). Experimental evidence of drift compressional waves in the magnetosphere: An Ekaterinburg coherent decameter radar case study. *Journal of Geophysical Research: Space Physics*, *121*(2), 1315–1326. https://doi.org/10.1002/2015ja022155

Chelpanov, M. A., Mager, P. N., Klimushkin, D. Y., & Mager, O. V. (2019). Observing magnetospheric waves propagating in the direction of electron drift with Ekaterinburg Decameter Coherent Radar. *Solar-Terrestrial Physics*, *5*(1), 51–57. https://doi.org/10.12737/stp-51201907

Chisham, G. (1996). Giant pulsations: An explanation for their rarity and occurrence during geomagnetically quiet times. *Journal of Geophysical Research: Space Physics*, *101*(A11), 24755–24763. https://doi.org/10.1029/96ja02540

Chisham, G., Lester, M., Milan, S. E., Freeman, M. P., Britow, W. A., Grocott, A., et al. (2007). A decade of the Super Dual Auroral Radar Network (SuperDARN): Scientific achievements, new techniques and future directions. *Surveys in Geophysics*, *28*(1), 33–109. https://doi.org/10.1007/s10712-007-9017-8

Chisham, G., Orr, D., & Yeoman, T. K. (1992). Observations of a giant pulsation across an extended array of ground magnetometers and on auroral radar. *Planetary and Space Science*, *40*(7), 953–964. https://doi.org/10.1016/0032-0633(92)90135-b

Dai, L., Takahashi, K., Wygant, J. R., Chen, L., Bonnell, J., Cattell, C. A., et al. (2013). Excitation of poloidal standing Alfvén waves through drift resonance wave-particle interaction. *Geophysical Research Letters*, *40*(16), 4127–4132. https://doi.org/10.1002/grl.50800

Di Matteo, S., Villante, U., Viall, N., Kepko, L., & Wallace, S. (2022). On differentiating multiple types of ULF magnetospheric waves in response to solar wind periodic density structures. *Journal of Geophysical Research: Space Physics*, *127*(3), e2021JA030144. https://doi.org/10.1029/2021ja030144

Elsden, T., & Wright, A. (2020). Evolution of high-m poloidal Alfvén waves in a dipole magnetic field. *Journal of Geophysical Research: Space Physics*, *125*(8), e2020JA028187. https://doi.org/10.1029/2020ja028187

Fenrich, F., Samson, J., Sofko, G., & Greenwald, R. (1995). ULF high-and low-*m* field line resonances observed with the Super Dual Auroral Radar Network. *Journal of Geophysical Research*, *100*(A11), 21535–21547. https://doi.org/10.1029/95ja02024

Gauld, J. K., Yeoman, T. K., Davies, J. A., Milan, S. E., & Honary, F. (2002). SuperDARN radar HF propagation and absorption response to the substorm expansion phase. *Annales Geophysicae*, *20*(10), 1631–1645. https://doi.org/10.5194/angeo-20-1631-2002

Grant, I., McDiarmid, D., & McNamara, A. (1992). A class of high-m pulsations and its auroral radar signature. *Journal of Geophysical Research: Space Physics*, *97*(A6), 8439–8451. https://doi.org/10.1029/92ja00434

Greenwald, R. A., Baker, K. B., Dudeney, J. R., Pinnock, M., Jones, T. B., Thomas, E. C., et al. (1995). DARN/SuperDARN: A global view of the dynamics of high-latitude convection. *Space Science Reviews*, *71*(1), 761–796. https://doi.org/10.1007/bf00751350

Hao, Y., Zong, Q.-G., Wang, Y., Zhou, X.-Z., Zhang, H., Fu, S., et al. (2014). Interactions of energetic electrons with ULF waves triggered by interplanetary shock: Van Allen Probes observations in the magnetotail. *Journal of Geophysical Research: Space Physics*, *119*(10), 8262–8273. https://doi.org/10.1002/2014ja020023

Hughes, W. J., & Southwood, D. J. (1976). The screening of micropulsation signals by the atmosphere and ionosphere. *Journal of Geophysical Research*, *81*(19), 3234–3240. https://doi.org/10.1029/ja081i019p03234

Hughes, W. J., Southwood, D. J., Mauk, B., McPherron, R. L., & Barfield, J. N. (1978). Alfvén waves generated by an inverted plasma energy distribution. *Nature*, *275*(5675), 43–45. https://doi.org/10.1038/275043a0

IMAGE. (2019). International monitor for auroral geomagnetic effects (IMAGE) stations coordinates. Retrieved from https://space.fmi.fi/image/www/index.php?page=stations)

Jacobs, J., Kato, Y., Matsushita, S., & Troitskaya, V. (1964). Classification of geomagnetic micropulsations. *Journal of Geophysical Research*, *69*(1), 180–181. https://doi.org/10.1029/jz069i001p00180

James, M. K., Yeoman, T. K., Mager, P. N., & Klimushkin, D. Y. (2013). The spatio-temporal characteristics of ULF waves driven by substorm injected particles. *Journal of Geophysical Research: Space Physics*, *118*(4), 1737–1749. https://doi.org/10.1002/jgra.50131

James, M. K., Yeoman, T. K., Mager, P. N., & Klimushkin, D. Y. (2016). Multiradar observations of substorm-driven ULF waves. *Journal of Geophysical Research: Space Physics*, *121*(6), 5213–5232. https://doi.org/10.1002/2015ja022102

Karpman, V., Meerson, B., Mikhailovsky, A., & Pokhotelov, O. (1977). The effects of bounce resonances on wave growth rates in the magnetosphere. *Planetary and Space Science*, *25*(6), 573–585. https://doi.org/10.1016/0032-0633(77)90064-2

Kepko, L., McPherron, R., Amm, O., Apatenkov, S., Baumjohann, W., Birn, J., et al. (2015). Substorm current wedge revisited. *Space Science Reviews*, *190*(1–4), 1–46. https://doi.org/10.1007/s11214-014-0124-9

Klimushkin, D. Y., Mager, P. N., & Glassmeier, K.-H. (2004). Toroidal and poloidal Alfvén waves with arbitrary azimuthal wavenumbers in a finite pressure plasma in the Earth's magnetosphere. *Annals of Geophysics*, *22*(1), 267–287. https://doi.org/10.5194/angeo-22-267-2004

Klimushkin, D. Y., Mager, P. N., Zong, Q., & Glassmeier, K.-H. (2019). Alfvén wave generation by a compact source moving on the magnetopause: Asymptotic solution. *Journal of Geophysical Research: Space Physics*, *124*(4), 2720–2735. https://doi.org/10.1029/2018ja025801

Kostarev, D. V., Mager, P. N., & Marep, П. (2017). Drift-compression waves propagating in the direction of energetic electron drift in the magnetosphere. *Solar-Terrestrial Physics*, *3*(3), 18–27. https://doi.org/10.12737/stp-33201703

Lessard, M., Hudson, M., & Lühr, H. (1999). A statistical study of Pc3–Pc5 magnetic pulsations observed by the AMPTE/Ion Release Module satellite. *Journal of Geophysical Research*, *104*(A3), 4523–4538.

Mager, O. V., Chelpanov, M. A., Mager, P. N., Klimushkin, D. Y., & Berngardt, O. I. (2019). Conjugate ionosphere-magnetosphere observations of a sub-Alfvénic compressional intermediate-m wave: A case study using EKB radar and van allen probes. *Journal of Geophysical Research: Space Physics*, *124*(5), 3276–3290. https://doi.org/10.1029/2019ja026541

Mager, P. N., & Klimushkin, D. Y. (2007). Generation of Alfvén waves by a plasma inhomogeneity moving in the Earth's magnetosphere. *Plasma Physics Reports*, *33*(5), 391–398. https://doi.org/10.1134/s1063780x07050042

Mager, P. N., & Klimushkin, D. Y. (2008). Alfvén ship waves: High-*m* ULF pulsations in the magnetosphere generated by a moving plasma inhomogeneity. *Annals of Geophysics*, *26*(6), 1653–1663. https://doi.org/10.5194/angeo-26-1653-2008

Mager, P. N., Klimushkin, D. Y., & Ivchenko, N. (2009). On the equatorward phase propagation of high-*m* ULF pulsations observed by radars. *Journal of Atmospheric and Solar-Terrestrial Physics*, *71*(16), 1677–1680. https://doi.org/10.1016/j.jastp.2008.09.001

Mann, I., Milling, D., Rae, I., Ozeke, L., Kale, A., Kale, Z., et al. (2008). The upgraded CARISMA magnetometer array in the THEMIS era. *Space Science Reviews*, *141*(1–4), 413–451. https://doi.org/10.1007/s11214-008-9457-6

Menk, F. W., & Waters, C. L. (2013). *Magnetoseismology: Ground-based remote sensing of Earth's magnetosphere*. John Wiley and Sons.

Milan, S., Jones, T., Lester, M., Warrington, E., & Reeves, G. (1996). Substorm correlated absorption on a 3200 km trans-auroral HF propagation path. *Annales Geophysicae*, *14*(2), 182–190. https://doi.org/10.1007/s00585-996-0182-8

Milan, S. E., Davies, J. A., & Lester, M. (1999). Coherent HF radar backscatter characteristics associated with auroral forms identified by incoherent radar techniques: A comparison of CUTLASS and EISCAT observations. *Journal of Geophysical Research*, *104*(A10), 22591–-22604. https://doi.org/10.1029/1999ja900277

Motoba, T., Kikuchi, T., Okuzawa, T., & Yumoto, K. (2003). Dynamical response of the magnetosphere-ionosphere system to a solar wind dynamic pressure oscillation. *Journal of Geophysical Research: Space Physics*, *108*(A5), 1206. https://doi.org/10.1029/2002ja009696

Mtumela, Z., Stephenson, J. A., & Walker, A. D. (2015). An investigation of the nature of a Pc5 pulsation event using Superdarn and magnetometer data. *South African Journal of Science*, *111*(3–4), 1–7. https://doi.org/10.17159/sajs.2015/20130391

Murphy, K. R., Inglis, A. R., Sibeck, D. G., Rae, I. J., Watt, C. E., Silveira, M., et al. (2018). Determining the mode, frequency, and azimuthal wave number of ULF waves during a HSS and moderate geomagnetic storm. *Journal of Geophysical Research: Space Physics*, *123*(8), 6457–6477. https://doi.org/10.1029/2017ja024877

Nishitani, N., Ruohoniemi, J. M., Lester, M., Baker, J. B. H., Koustov, A. V., Shepherd, S. G., et al. (2019). Review of the accomplishments of mid-latitude Super Dual Auroral Radar Network (SuperDARN) HF radars. *Progress in Earth and Planetary Science*, *6*(27), 1–57. https://doi.org/10.1186/s40645-019-0270-5

Radoski, H. R. (1974). A theory of latitude dependent geomagnetic micropulsations: The asymptotic fields. *Journal of Geophysical Research*, *79*(4), 595–603. https://doi.org/10.1029/ja079i004p00595

Rae, I., Donovan, E., Mann, I., Fenrich, F., Watt, C., Milling, D., et al. (2005). Evolution and characteristics of global Pc5 ULF waves during a high solar wind speed interval. *Journal of Geophysical Research: Space Physics*, *110*(A12), A12211. https://doi.org/10.1029/2005ja011007

Sarris, T., Wright, A., & Li, X. (2009). Observations and analysis of Alfvén wave phase mixing in the Earth's magnetosphere. *Journal of Geophysical Research: Space Physics*, *114*(A3), A03218. https://doi.org/10.1029/2008ja013606

Southwood, D. J. (1976). A general approach to low-frequency instability in the ring current plasma. *Journal of Geophysical Research*, *81*(19), 3340–3348. https://doi.org/10.1029/ja081i019p03340

Southwood, D. J., Dungey, J. W., & Etherington, R. J. (1969). Bounce resonant interaction between pulsations and trapped particles. *Planetary and Space Science*, *17*(3), 349–361. https://doi.org/10.1016/0032-0633(69)90068-3

Southwood, D. J., & Kivelson, M. G. (1982). Charged particle behavior in low-frequency geomagnetic pulsations, 2. graphical approach. *Journal of Geophysical Research*, *87*(A3), 1707–1710. https://doi.org/10.1029/ja087ia03p01707

Stern, D. P. (1975). The motion of a proton in the equatorial magnetosphere. *Journal of Geophysical Research*, *80*(4), 595–599. https://doi.org/10.1029/ja080i004p00595

Takahashi, K., Claudepierre, S. G., Rankin, R., Mann, I. R., & Smith, C. W. (2018). Van Allen Probes observation of a fundamental poloidal standing Alfvén wave event related to giant pulsations. *Journal of Geophysical Research: Space Physics*, *123*(6), 4574–4593. https://doi.org/10.1029/2017ja025139

Takahashi, K., Denton, R. E., Anderson, R. R., & Hughes, W. J. (2004). Frequencies of standing alfvén wave harmonics and their implication for plasma mass distribution along geomagnetic field lines: Statistical analysis of crres data. *Journal of Geophysical Research: Space Physics*, *109*(A8), A08202. https://doi.org/10.1029/2003ja010345

Takahashi, K., & McPherron, R. L. (1984). Standing hydromagnetic oscillations in the magnetosphere. *Planetary and Space Science*, *32*(11), 1343–1359. https://doi.org/10.1016/0032-0633(84)90078-3

Tian, M., Yeoman, T. K., Lester, M., & Jones, T. B. (1991). Statistics of Pc 5 pulsation events observed by SABRE. *Planetary and Space Science*, *39*(9), 1239–1247. https://doi.org/10.1016/0032-0633(91)90037-b

Tsyganenko, N. A. (1996). Effects of the solar wind conditions in the global magnetospheric configurations as deduced from data-based field models. *International conference on substorms*, *389*, 181.

Volland, H. (1973). A semiempirical model of large-scale magnetospheric electric fields. *Journal of Geophysical Research*, *78*(1), 171–180. https://doi.org/10.1029/ja078i001p00171

Wright, D. M., & Yeoman, T. K. (1999). High resolution bistatic HF radar observations of ULF waves in artificially generated backscatter. *Geophysical Research Letters*, *26*(18), 2825–2828. https://doi.org/10.1029/1999gl900606

Yeoman, T., & Lühr, H. (1998). Cutlass/image observations of high latitude convection features during substorms. *Advances in Space Research*, *22*(9), 1293–1296. https://doi.org/10.1016/s0273-1177(98)00174-4

Yeoman, T. K., Baddeley, L. J., Dhillon, R. S., Robinson, T. R., & Wright, D. M. (2008). Bistatic observations of large and small scale ULF waves in SPEAR-induced HF coherent backscatter. *Annals of Geophysics*, *26*(8), 2253–2263. https://doi.org/10.5194/angeo-26-2253-2008

Yeoman, T. K., James, M. K., Klimushkin, D. Y., & Mager, P. N. (2016). *Energetic particle-driven ULF waves in the ionosphere*. In A. Keiling, D. Lee, & V. Nakariakov (Eds.), *Low-frequency waves in space plasmas* (Vol. 216, pp. 1–14). American Geophysical Union (AGU).

Yeoman, T. K., James, M. K., Mager, P. N., & Klimushkin, D. Y. (2012). SuperDARN observations of high-*m* ULF waves with curved phase fronts and their interpretation in terms of transverse resonator theory. *Journal of Geophysical Research: Space Physics*, *117*(A6), A06231. https://doi.org/10.1029/2012ja017668

Yeoman, T. K., Klimushkin, D. Y., & Mager, P. N. (2010). Intermediate-*m* ULF waves generated by substorm injection: A case study. *Annals of Geophysics*, *28*(8), 1499–1509. https://doi.org/10.5194/angeo-28-1499-2010

Yeoman, T. K., Tian, M., Lester, M., & Jones, T. B. (1992). A study of Pc5 hydromagnetic waves with equatorward phase propagation. *Planetary and Space Science*, *40*(6), 797–810. https://doi.org/10.1016/0032-0633(92)90108-z

Yeoman, T. K., & Wright, D. M. (2001). ULF waves with drift resonance and drift-bounce resonance energy sources as observed in artificially-induced HF radar backscatter. *Annals of Geophysics*, *19*(2), 159–170. https://doi.org/10.5194/angeo-19-159-2001

Yeoman, T. K., Wright, D. M., & Baddeley, L. J. (2006). Ionospheric signatures of ULF waves: Active radar techniques. In K. Takahashi, P. J. Chi, R. E. Denton, & R. L. Lysak (Eds.), *Magnetospheric ULF waves: Synthesis and new directions, Geophysical Monograph Series*, (Vol. 169, pp. 273–288). American Geophysical Union.

Yumoto, K. (1988). External and internal sources of low-frequency MHD waves in the magnetosphere: A review. *Journal of Geomagnetism and Geoelectricity*, *40*(3), 293–311. https://doi.org/10.5636/jgg.40.293

Zolotukhina, N. A., Mager, P. N., & Klimushkin, D. Y. (2008). Pc5 waves generated by substorm injection: A case study. *Annals of Geophysics*, *26*(7), 2053–2059. https://doi.org/10.5194/angeo-26-2053-2008